



Contents lists available at ScienceDirect

International Journal of Plasticity

journal homepage: <http://www.elsevier.com/locate/ijplas>



A machine learning framework to predict local strain distribution and the evolution of plastic anisotropy & fracture in additively manufactured alloys

Waqas Muhammad ^{a,b}, Abhijit P. Brahme ^a, Olga Ibragimova ^a, Jidong Kang ^b,
Kaan Inal ^{a,*}

^a Department of Mechanical and Mechatronics Engineering, University of Waterloo, Waterloo, N2L 3G1, Canada

^b CanmetMATERIALS, 183 Longwood Road South, Hamilton, L8P 0A5, Canada



ARTICLE INFO

Keywords:

Artificial intelligence
Machine learning
Selective laser melting
Plastic anisotropy
Fracture

ABSTRACT

Machine learning (ML) approaches are widely used to develop systems or frameworks with the ability to predict the properties of interest by learning and establishing relationships and inferences from data. In the present work, an ML based framework is proposed to predict the evolution of local strain distribution, plastic anisotropy and failure during tensile deformation of AlSi10Mg aluminum alloy produced by selective laser melting (SLM). The framework combines the methods involved in additive manufacturing (AM) and artificial intelligence (AI). This includes printing of test specimens using laser powder bed fusion (LPBF), x-ray computed tomography (CT) scanning to measure internal defects distribution, mechanical testing with digital image correlation (DIC) to get local strain evolution, extraction and coupling of CT and DIC data, and the development, validation and evaluation of an artificial neural network (ANN) model. The experimental data from CT and DIC measurements are used to train, validate and evaluate the proposed ANN model. Microstructural features such as the size, shape, volume fraction and distribution of porosity are used as an input to ANN. The proposed ANN model successfully predicts the evolution of local strains, plastic anisotropy and failure during tensile deformation. The intensity and location of strain hotspots as well as the shape of shear bands and the location of crack initiation are well predicted. The current research demonstrates the applicability of an ML based ANN approach to predict microstructure – property – performance relationships for engineering materials with intricate heterogeneous microstructures such as those produced additively by SLM. The success of the present approach motivates further use of ML techniques, as a mean for accelerated development of new alloys, AM process optimization and its wide scale applicability.

1. Introduction

Additive manufacturing (AM), also known as 3D printing, is a state-of-the-art technology enabling fabrication of complex geometries and near net-shape parts with minimal raw material utilization (Bonatti and Mohr, 2017; Bronkhorst et al., 2019; Gao et al.,

* Corresponding author.

E-mail address: kinal@uwaterloo.ca (K. Inal).

2015; Ghorbanpour et al., 2017; Tancogne-Dejean et al., 2016; Zhang and To, 2016). Over the past decade, additive printing methods such as selective laser melting (SLM) or laser powder bed fusion (LPBF) has shown significant promise and manufacturing potential. The method applies a high power-density laser to selectively melt and fuse metallic powder together while building part layer-by-layer, without requiring any part-specific tooling. This allows for rapid prototyping, shortening of design and production cycle while offering significant time and cost savings (Z. X. Li et al., 2019; Olakanmi et al., 2015; Wang et al., 2019). However, one of the major concerns in AM build parts is the variation in the microstructure along with the process induced defects such as porosity and surface roughness (Ali et al., 2019a; Ghorbanpour et al., 2020; Li et al., 2020; Liu et al., 2017; Pokharel et al., 2019; Witzen et al., 2020). The mechanical properties of these materials are strongly governed by the choice of process parameters employed during the fabrication process (Ferreri et al., 2019; Hadadzadeh et al., 2019; Hitzler et al., 2017; Ku et al., 2020; Liu et al., 2020; Tang and Pistorius, 2017; Zaretsky et al., 2017). Akin to metal parts manufactured using conventional methods, AM parts would also typically experience plasticity during their service life. Therefore, understanding their mechanical – plastic deformation behavior is essential for their wide scale applicability.

Several studies have been performed to understand the mechanical behavior of LPBF printed AlSi10Mg Aluminum alloys (Asgari et al., 2017; Brandl et al., 2012; Li et al., 2016, 2020; Read et al., 2015; Rosenthal et al., 2018; Thijs et al., 2013; Wei et al., 2017). A significant directional anisotropy in the tensile and compressive loading behaviors of AlSi10Mg alloy has been reported by many researchers (Hitzler et al., 2017; Liu et al., 2018; Tang and Pistorius, 2017). Kempen et al. (2012) investigated the elongation to failure of AlSi10Mg tensile specimens produced by SLM. The authors observed a significant discrepancy in the total elongation at break amongst specimens and attributed this behavior to the difference in the underlying process induced porosity within specimens. Rosenthal et al. (2017) studied the strain rate sensitivity of AlSi10Mg and reported a significant increase in flow stress directional anisotropy for strain rates between $2.77 \times 10^{-6} \text{ s}^{-1}$ to $2.77 \times 10^{-1} \text{ s}^{-1}$. The orientation dependence of mechanical properties such as yield stress, tensile strength, hardening exponent, and elongation to failure of AlSi10Mg alloy are linked with the inhomogeneities induced by SLM manufacturing technology. Kempen et al. (2015) performed a SLM process control optimization study using AlSi10Mg alloy. The authors reported that the tensile properties of the material are strongly influenced by laser power, scanning speed, scan pattern and layer thickness and showed that by optimizing the process, one can print nearly fully dense parts with superior mechanical properties.

It is known that a wide variety of synergistic factors can significantly influence the elasto-plastic behavior of AM parts. In addition to the laser processing parameters, these include the effects of surface roughness, residual stresses, defects such as porosity and lack of

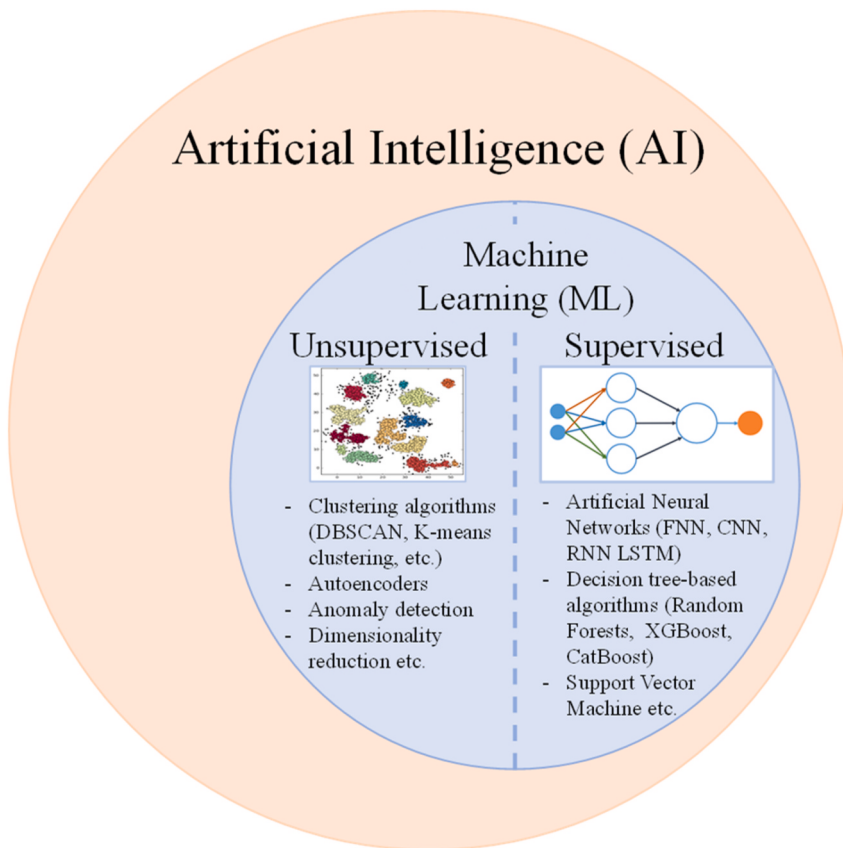


Fig. 1. Artificial intelligence and machine learning.

fusion defects (Ali et al., 2017; Calignano, 2018; Csanádi et al., 2014; Grasso and Colosimo, 2017; Khairallah et al., 2016; Khan and Liu, 2012; Read et al., 2015; Wei et al., 2017; Yan et al., 2016). Therefore, understanding the linkages between process parameters, resulting microstructure and mechanical performance is of extreme importance for AM process optimization and its wide scale applicability. In these regards, artificial intelligence (AI) based machine learning (ML) tools are key enablers for accelerated development of new materials, manufacturing processes and methods. The application of such approaches in the field of material science is becoming more common with an aim to achieve high-throughput identification and quantification of essential material parameters or salient features along the process-microstructure-property-performance chain (Dobrzański and Honysz, 2009; Kiselyova et al., 1998; Olakanmi et al., 2015). Therefore, the use of ML approaches coupled with AM processes would provide an excellent medium for scale-bridging, and understanding - establishing linkages between process parameters, microstructural features, the resulting mechanical characteristics such as large strain elasto-plastic behavior, failure and fracture.

Machine learning (ML) is a sub-field of artificial intelligence that aims to perform a task of interest by analyzing and learning hidden links and patterns within a given data-set. A schematic representation of some of the common ML approaches is given in Fig. 1. The approaches are classified as supervised (where the algorithm learns from labeled training data and helps in predicting outcomes for unforeseen data) and unsupervised learning (where the algorithm discovers and establishes relationships amongst features of interest on its own by dealing with unlabelled data). Using ML approaches, one can develop systems or frameworks with the ability to automatically learn and improve by establishing relationships and inference from data, without being explicitly programmed (Lecun et al., 2015; Liu et al., 2017).

To date, there has been numerous successful applications of machine learning for image classification, computer vision, autonomous driving, fraud detection and virtual assistants (Flach, 2012; Goodfellow et al., 2016). ML approaches have also been applied in the field of computational mechanics and materials science, specifically metal plasticity, to improve modeling predictions, reduce computational time and minimize experimental costs (Bock et al., 2019; Mangal and Holm, 2018; Schmidt et al., 2019; Zhang and Ling, 2018). Some of the early works apply artificial neural networks (ANNs) to train and predict the constitutive response of engineering materials. For instance, Qin et al. (2010) used feed-forward back propagation artificial neural network with single hidden layer and 23 neurons to model the hot compression behavior of ZK60 magnesium alloy in the temperature range of 200–400 °C and strain rate range of 0.001–1 s⁻¹. Similarly, Jenab et al. (2016) used ANN to successfully predict the tensile flow behavior of AA5182-O sheet material in different test directions for strain rates ranging from 0.001 to 1000 s⁻¹. More recently, Z. Li et al. (2019) used neural network approach with three hidden layers of 10 neurons each to develop a modified Johnson-Cook model for describing the strain rate and temperature dependent plasticity of DP steels. ML algorithms have also been used to predict the onset of necking for metal forming applications. Elangovan et al. (2010) used a feed forward neural network to successfully predict the forming limit diagram (FLD) of commercially pure aluminum perforated sheets. Derogar and Djavanroodi (2011) used a neural network with one hidden layer containing 4 neurons to predict the limiting strains for Ti6Al4 V titanium and Al6061-T6 aluminum alloy sheets. Similarly, Kotkunde et al. (2014) developed a neural network framework to model the deep drawing process. The authors used a neural network with one hidden layer featuring 20 neurons to predict the major and minor strain evolution of a Ti-6Al-4V alloy during deep drawing. Some of the recent applications of ANN are aimed towards developing frameworks to capture the multi-axial aspects of plasticity. Ali et al. (2019b) proposed an ANN based framework with single hidden layer to predict the stress-strain response of polycrystalline materials subjected to multiaxial as well as non-proportional loading conditions. The authors coupled ANN model with a rate-dependant crystal plasticity finite element method (CPFEM) to successfully predict the constitutive response of AA6063-T6 under complex loading paths such as tension followed by simple shear. The proposed framework also accounted for texture evolution during deformation and provided a substantial computational speedup compared to conventional crystal plasticity methods. More recently, Zhang and Mohr (2020) proposed a neural network based mises-plasticity model with isotropic hardening. The authors used a fully-connected feedforward network with five hidden layers with 15 neurons per layer to describe the plane stress plasticity condition. The model was implemented within a finite element framework and it was shown that the elasto-plastic response of a von Mises material can be captured through a neural network without any explicit use of the yield function, flow rule or hardening laws.

Majority of the published works on the elasto-plastic behavior of 3D printed AlSi10Mg aluminum alloys are focused on characterizing and understating the origins of directional anisotropy in the tensile or compressive stress-strain response of the alloy. However, to the best knowledge of authors, there are no works on studying the evolution of local strain distribution, plastic anisotropy, and failure during plastic deformation and their link to the process induced porosity within the 3D printed material. Furthermore, there are no existing works on the predictive capability of machine learning based ANN models to capture the local strain heterogeneities observed in additively printed materials during plastic deformation.

The current research seeks to integrate the advancements in the field of artificial intelligence and laser powder bed fusion (LPBF) based additive manufacturing to enable accelerated development of new aluminum alloys by identifying linkages between essential microstructural parameters and the resulting mechanical performance. The purpose of the current work is twofold. Firstly, an experimental investigation will be conducted to study the linkages between the tensile deformation behavior and the process induced porosity for AlSi10Mg alloy produced by SLM. Specifically, the relationship between local porosity distribution and the evolution of local strains, plastic anisotropy and failure during tensile loading is investigated. Next, an ANN based framework will be developed with an aim to predict the local strain distribution and the evolution of plastic anisotropy and failure during tensile deformation of AlSi10Mg alloy. As such, a successful implementation of the model would help in development of a framework for predicting experimental trends in materials with complex heterogeneous microstructures and would eventually help in promoting the application of AI in AM.

2. Experimental characterization

2.1. Fabrication of tensile specimens

Standard ASTM-E8M subsize tensile specimens (see Fig. 2) having thickness of 1.2 mm, were printed using Renishaw AM400 system equipped with a $250 \times 250 \times 300$ mm build platform and a 400 W Yttrium fibre laser. The laser processing parameters for the build are given in Table 1. The specimens were fabricated to net-shape using a pre-alloyed AlSi10Mg powder with a particle size range of 20–45 μm . The nominal composition of the powder is given in Table 2. The fabrication process was carried out in an inert atmosphere (i.e. Argon) with an oxygen content of less than 0.1%. The build platform temperature was set at 170 °C during fabrication. Fig. 3 shows a schematic representation of the orientation of different specimens with respect to the build direction (Z) on the base plate. In total, 10 specimens per direction were printed. However, for clarity only 3 specimens per direction are shown and each of the five printing directions are labeled as X00, X90, Y00, Y90 and XY90 in Fig. 3.

2.2. X-ray computed tomography

X-ray micro computed tomography (CT) measurements were performed to analyze the porosity distribution within the as-fabricated specimens. The CT scans were performed using Zeiss Xradia 520 Versa which can provide a true spatial resolution of 0.7 μm with a minimum achievable voxel size of 70 nm. In the present work, the CT scans were performed using a voxel size of 2 μm . The stack-wise image data from CT scans was further processed to obtain a full 3D reconstruction of internal porosity distribution.

2.3. Mechanical testing

Tensile tests were conducted to characterize the mechanical behavior of the printed specimens. The tests were performed at room temperature using an MTS Landmark 370 Servo-hydraulic tensile machine with a load cell capacity of 30 KN. A quasi-static strain rate of $5 \times 10^{-4}/\text{s}$ was employed, and each test was repeated three times to ensure reproducibility and accuracy of experimental data. Furthermore, a digital image correlation (DIC) system was used to capture speckled deformed images of the gage section of the tensile specimen during testing. The DIC data was further analyzed using the commercial software VIC-2D® to extract local strain evolution during tensile deformation. The resolution of the DIC image was approximately 0.02 mm/pixel. The Hencky (logarithmic) strain was computed and smoothed using a gaussian decay filter with filter size of 6.

In the present work, the plastic anisotropy of the materials is quantified using the plastic strain ratio or the r-value. The r-value indicates the ability of the material to resist thinning and is therefore an important indicator of plastic deformation behavior of the material (Kang and Muhammad (2017)). It is commonly defined as

$$r = \frac{\varepsilon_w}{\varepsilon_t} = -\frac{\varepsilon_w}{\varepsilon_l + \varepsilon_w} \quad (1)$$

where ε_l , ε_w , and ε_t are the longitudinal, width and thickness strains, respectively. The r-values are calculated using the local strain measurements obtained through DIC, in accordance with the ASTM-E517-19. The values are calculated using the point method (as outlined in Muhammad et al. (2016) and Kang and Muhammad (2017)) at three different locations (i.e. 1/4th, 1/2, and 3/4th) along the gage length of the specimen.

2.4. Microstructure characterization

It is well-known that additively manufactured materials can exhibit complex heterogeneous microstructures. In the present study, this microstructural heterogeneity is characterized using electron backscatter diffraction (EBSD) measurements. For this purpose, one of the X00 specimens is sectioned along different planes to observe the microstructure within the gage region of the specimen. Fig. 4 shows a schematic of X00 specimen, where LD represents the loading direction, TD represents transverse to the loading direction and BD represents the build direction. Three EBSD measurements were performed. One each on the top and bottom surfaces within the gage region along the LD-TD plane. The third measurement was performed along the LD-BD plane to characterize the through thickness microstructure. The EBSD specimens were prepared using standard metallography techniques followed by ion-milling to

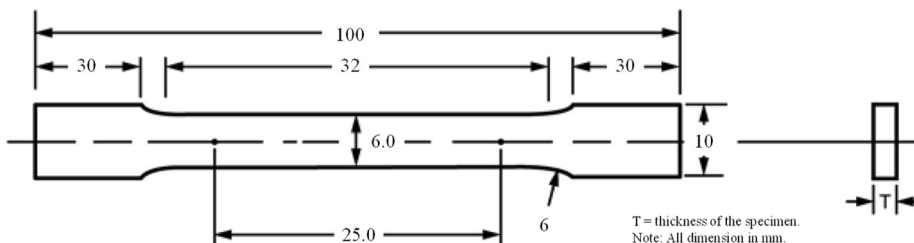


Fig. 2. ASTM E8M subsize tensile specimen geometry.

Table 1
SLM processing parameters.

Power (W)	Point Distance (μm)	Velocity(mm/s)	Spot size(μm)	Layer Thickness (μm)	Hatching Distance (μm)	Rotation Angle ($^{\circ}$)
350	50	650	100	30	90	67

Table 2
Chemical composition (max. wt%) of AlSi10Mg powder.

Si	Mg	Cu	Fe	Mn	Ni	Ti	Al
10.5	0.42	0.005	0.19	0.01	0.01	0.01	Bal.

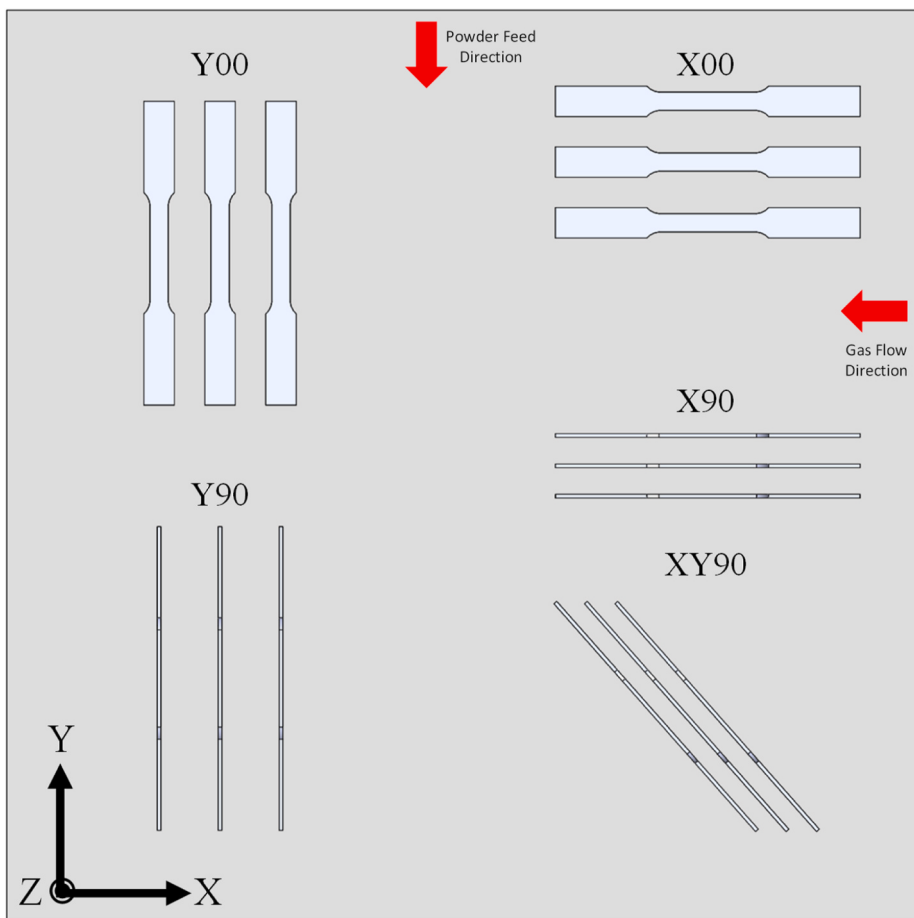


Fig. 3. Schematic of X00, X90, Y00, Y90 and XY90 tensile specimens with respect to build direction (Z).

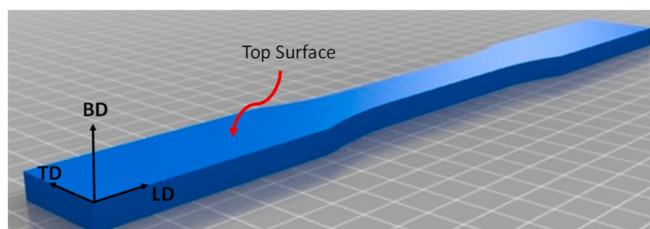


Fig. 4. Schematic of X00 specimen.

achieve the desired surface finish. The readers are referred to Muhammad et al. (2019b, 2019a) for more information on EBSD sample preparation. All texture measurements were made using a field-emission Zeiss N-Vision SEM equipped with a TSL EBSD camera. A step size of $0.5 \mu\text{m}$ was used for all EBSD measurements and the data was further processed using the TSL OIM™ software. The data is cleaned using neighbour CI correlation to remove bad data points within the TSL software.

2.5. Experimental results and discussion

EBSD inverse pole figure (IPF) maps of the top (LD-TD), bottom (LD-TD) and through thickness (LD-BD) planes are shown in Fig. 5. The grain morphology along the top and bottom surfaces of the specimen is equiaxed in nature with an average grain size of $5 \mu\text{m}$. However, it is noted that the actual 3D shape of the grains varies along the build direction of the specimen, as shown in Fig. 5(c). This through thickness grain morphology changes as a function of the distance from the build plate. The region closest to the build plate exhibits equiaxed grain morphology (see leftmost region in Fig. 5(c)). The grain morphology transitions from equiaxed to columnar with increasing distance from the base plate. The central region of the specimen exhibits a mixed of columnar-equiaxed grain morphology, whereas the morphology is columnar in vicinity of the top surface (i.e. rightmost region in Fig. 5(c)) of the specimen.

Apart from the heterogeneity in grain morphology, the through thickness texture also varies along the build direction. The columnar grains predominantly exhibit a near $<001>$ texture, whereas the $<101>$ and $<111>$ texture components are more apparent in equiaxed grains. This behavior is consistent with previously reported results in the literature (Garibaldi et al., 2016; Liu and To, 2017; Liu et al., 2018; Takata et al., 2018). This complexity and heterogeneity in the microstructure of the alloy results from variation in solidification conditions such as the variation in the cooling rate and thermal gradient along the build direction (Hadadzadeh et al., 2018).

Fig. 6 shows the engineering stress-strain curves of the AlSi10Mg specimens subjected to uniaxial tension. As mentioned previously, each test was repeated three times for the five different print orientations (i.e. X00, X90, Y00, Y90, XY90). The average yield stress, ultimate tensile strength (UTS), elongation to failure and the corresponding standard deviations are summarized in Table 3 for each print direction. It is observed that the specimens that were printed with flat side in-contact with the base plate (i.e. X00 and Y00 specimens) exhibit a similar yield strength, ultimate tensile strength, and the overall hardening behavior. The average yield stress for X00 and Y00 specimens is 148.1 MPa and 148.8 MPa respectively, and the average UTS for these specimens is 227.4 MPa and 229.1 MPa (see Table 3). On the contrary, all specimens that were printed with their edge or thickness being in-contact with the build plate (i.e. X90, Y90 and XY90 specimens) exhibit a similar tensile behavior with an average yield stress and UTS of approximately 135 MPa and 220 MPa, respectively. This directional anisotropy in the tensile stress-strain response of AlSi10Mg has been observed in the past, and is a consequence of an inhomogeneous temperature distribution and differences in heat conduction to the surrounding powder bed and build plate (Hitzler et al., 2017; Kempen et al., 2012; Tang and Pistorius (2017)). The tensile tests also show a difference in ductility or elongation to failure across all specimens. The difference in ductility is more pronounced for X00 and Y00 specimens, with X00 specimens exhibiting the lowest elongation to failure. The average elongation to failure for X00 specimens is 9.3% with a standard deviation of $\pm 1.15\%$. Since these specimens were printed with one of the flat faces being in-contact with the base plate, the larger

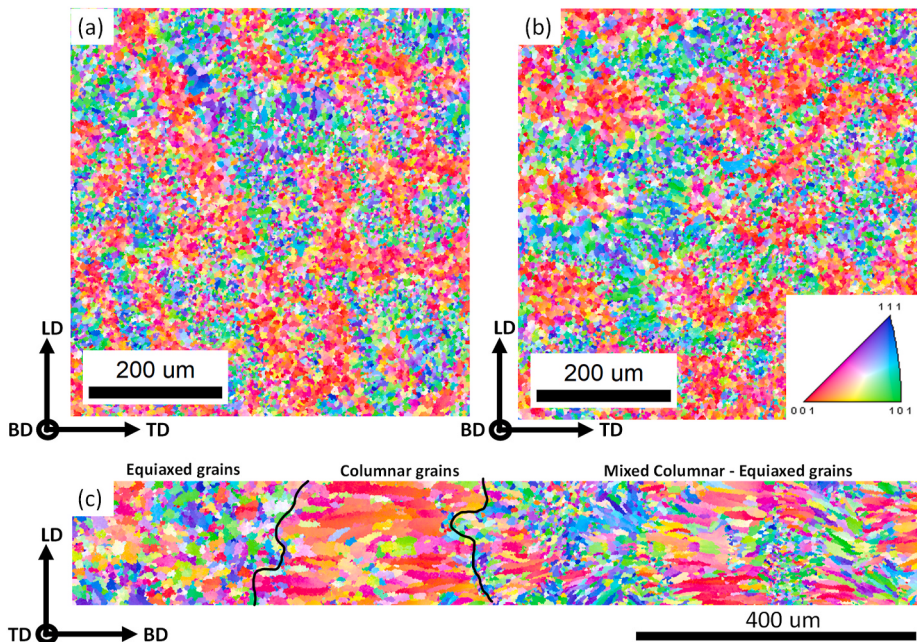


Fig. 5. Inverse pole figure (IPF) map showing the microstructure of X00 specimen within the gage region along the (a) top (b) bottom and (c) through thickness planes.

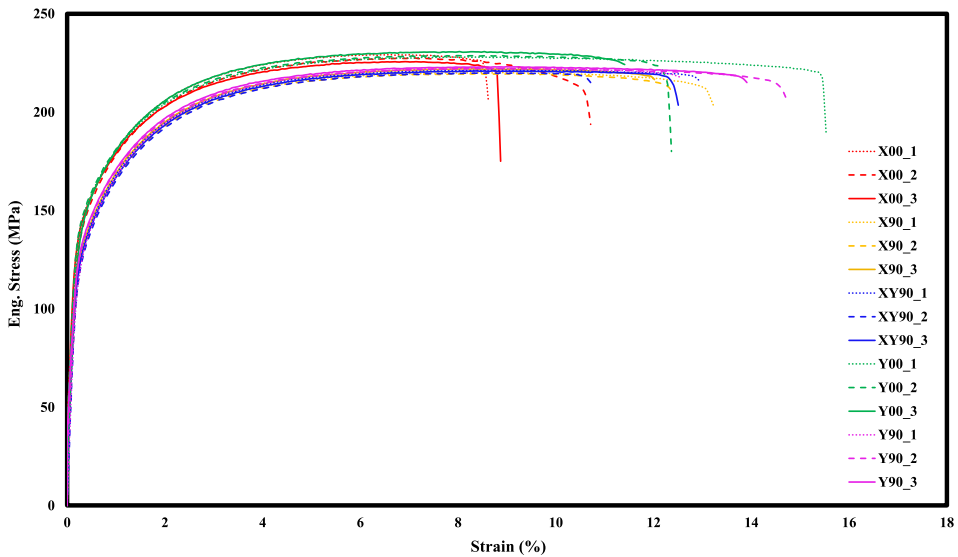


Fig. 6. Engineering stress vs engineering strain response of AlSi10Mg aluminum specimens.

Table 3

Average tensile yield stress, UTS and elongation to failure for AlSi10Mg specimens along X00, Y00, X90, Y90 and XY90 print directions.

Print Direction	Yield Stress (MPa)	UTS (MPa)	Elongation to Failure (%)
X00	148.1 ± 1.99	227.4 ± 1.79	9.3 ± 1.15
Y00	148.8 ± 1.53	229.1 ± 1.40	13.1 ± 2.18
X90	135.8 ± 2.26	220.2 ± 1.15	12.4 ± 0.63
Y90	136.5 ± 2.79	221.5 ± 0.37	13.7 ± 1.09
XY90	134.1 ± 1.90	220.3 ± 1.04	11.9 ± 1.16

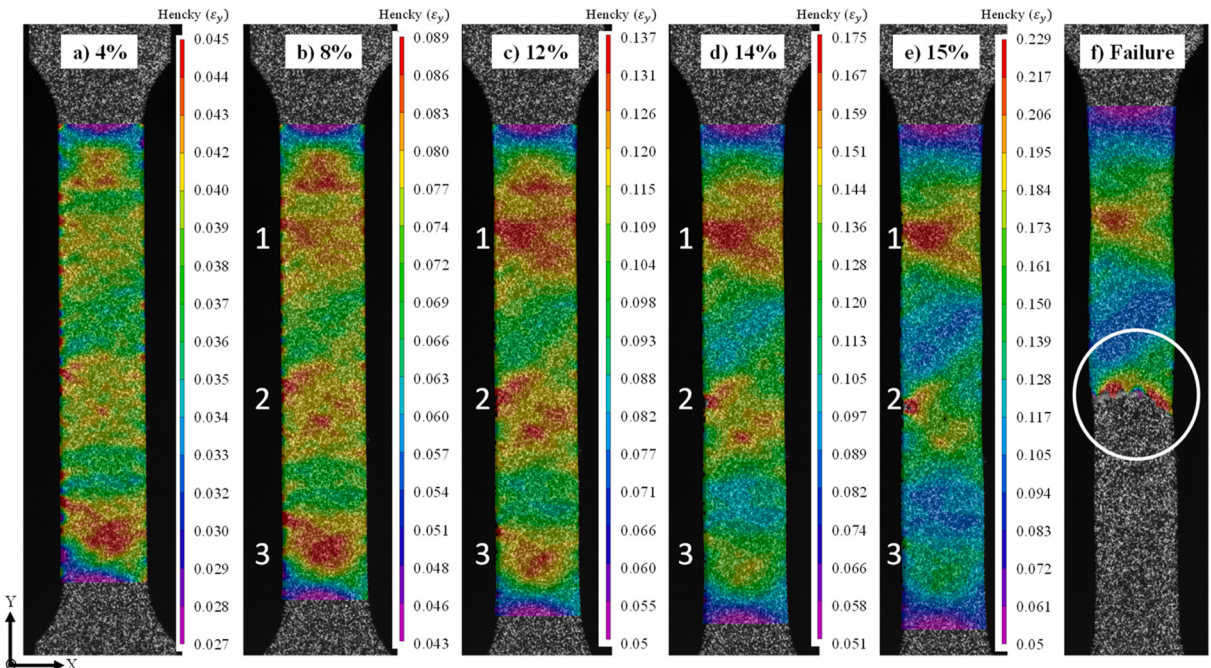


Fig. 7. DIC maps of strain evolution within the gage section of Y00-1 specimen at (a) 4%, (b) 8%, (c) 12%, (d) 14%, (e) 15% axial strain and (f) failure.

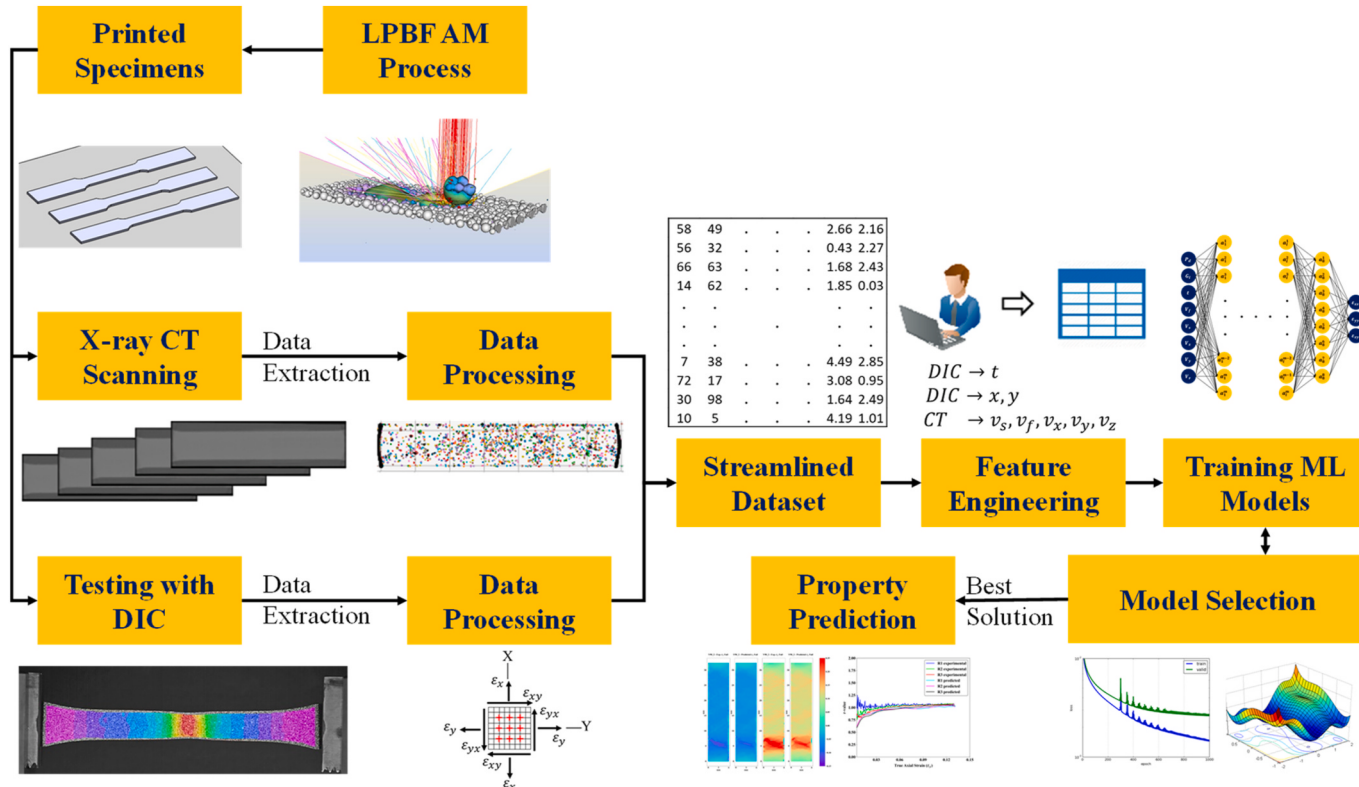


Fig. 8. Schematic representation of the proposed ML framework.

cross-sectional printing area per layer may facilitate a high area fraction of porosity near the top and bottom flat faces of the printed specimens, thereby reducing ductility. The porosity distribution across specimens is also affected by the location of the specimen on the build plate and the direction of the inert gas flow within the build chamber (Ali et al., 2019a; Hitzler et al., 2017). The highest average elongation to failure of 13.7% is observed for the Y90 specimens.

Fig. 7 shows the DIC maps for Hencky strain (ϵ_y) evolution at different intervals during tensile deformation of Y00_1 specimen. It is noted that the plastic deformation is heterogeneous even at a relatively low axial strain of 4% (see **Fig. 7 (a)**). One can see the presence of several strain hotspots at different locations within the gage length. This behavior is contrary to that observed for conventional wrought aluminum alloys, where strain distribution is comparatively uniform within the gage section up until the onset of necking (Kang and Muhammad (2017)). Furthermore, between 8% and 12% axial deformation, strain starts localizing at multiple different regions within the gage section as indicated by 1, 2 and 3 in **Fig. 7 (b)** and (c). Unlike conventional metals, this multi-localization behavior is believed to be unique to additively printed materials and is affected by the distribution of the inherent process induced porosity with the specimen. As deformation proceeds further, strain localization within region 1 becomes more intense whereas the opposite is true for region 3 (see **Fig. 7 (d)**). At 15% axial strain, multiple localization regions are present, and it is rather hard to determine the perceived location of failure. As such for this specimen, failure happens suddenly in the central region of the specimen and is promoted, most likely, by the near edge porosity.

In brief, the AlSi10Mg tensile specimens show a mild directional anisotropy for yield and ultimate tensile stresses. However, there is a significant discrepancy in the elongation to failure values across all specimens. Furthermore, unlike conventional metals, strain tends to localize across multiple regions within the gage section of the SLM printed AlSi10Mg alloy and the deformation is rather heterogeneous at the local scale, starting at a very early stage of plastic straining. This heterogeneous deformation behavior and the variation in ductility amongst specimens are linked with the underlying porosity distribution within the specimen. Therefore, it is vital to analyze and establish the linkages between this microstructural porosity distribution and the local strain evolution for proper understanding and prediction of the deformation behavior at the local scale for SLM printed AlSi10Mg alloy. In these regards, the porosity data from x-ray computed tomography will be combined with the local strain distribution data from DIC to study the deformation behavior. The data is further used for the development and validation of a machine learning based ANN model for prediction of local strain distribution, the evolution of plastic anisotropy and fracture.

3. Development of machine learning framework

The goal of the present work is to develop and implement a machine learning based framework to predict the local strain distribution, the evolution of plastic anisotropy and failure during tensile loading of AlSi10Mg aluminum alloy produced by SLM. The framework would couple the methods and procedures involved in additive manufacturing and artificial intelligence to enable prediction of local strain heterogeneities that are observed during plastic straining of AM materials with complex microstructures. **Fig. 8**

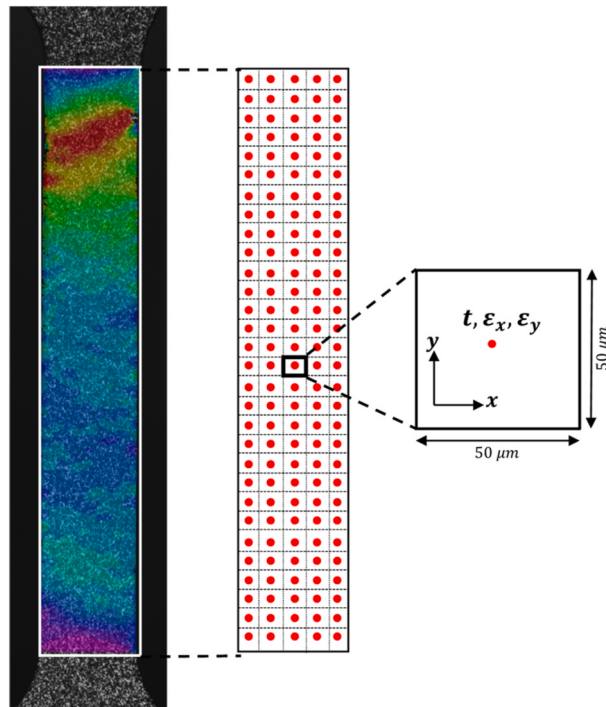


Fig. 9. Strain evolution data extraction from processed DIC images.

shows a generalized schematic of the proposed framework. The framework involves designing and printing of test specimens using LPBF technology, micro-CT scanning to measure internal porosity distribution and mechanical testing using DIC to obtain local strain evolution, extraction and coupling of numerical data from CT and DIC measurements, feature engineering to select a representative and compact set of features, machine learning model selection, training, validation and evaluation. The next few subsections provide details on dataset generation, feature engineering and machine learning model development.

3.1. Dataset generation

The feasibility of any machine learning algorithm and the quality of model predictions are strongly influenced by the size and accuracy of the input dataset ([Zhang and Ling \(2018\)](#)). It is vital that the input dataset contains enough information that is representative of the given problem. Hence, the dataset generation and collection processes lie at the core of a successful implementation of an ML framework. In the present work, the datasets including initial porosity distribution and local strain evolution during tensile deformation are obtained using x-ray computed tomography and digital image correlation methods, respectively. Both datasets are superimposed and combined to obtain a single streamlined dataset as discussed next.

I Processing of DIC Dataset.

The DIC images are processed using a commercial software VIC-2D® to obtain strain evolution maps during tensile deformation. The data points are extracted from the software as an x , y grid with each point representing a region of approx. $50 \mu\text{m}$ (see [Fig. 9](#)). Information such as deformation time t , grid point location x , y and local strain values ε_x and ε_y are extracted.

II Processing of X-ray CT Dataset using Unsupervised Learning.

As mentioned previously, the fabricated tensile specimens are CT scanned to obtain the location and distribution of voids within the gage section. The CT data is stored in a layer-wise series of flat 2D images. This data needs to be extracted from the images in a meaningful way so that it can be used for subsequent analysis. The extraction process can be broken down into different parts a) image correction and extraction of pixels that belong to voids b) aggregation of void pixels into voids and c) reconciliation with DIC data.

Since a perfect alignment of the tensile specimen with the scanning system is difficult, each CT image in series (i.e. slice), needs to be corrected for any misalignment. This misalignment is constant for a given specimen but might change across different specimens. Thus, for each tensile specimen, the rotation is calculated, and slices are rotated to proper reference frame. The identification of the rotation is not trivial as most image processing software, such as ImageJ, do not give the option to rotate the data below a certain tolerance. Hence, a custom code is written and applied to each stack separately to identify the amount of rotation, which is then applied to the stack to realign the specimen. The CT scan data is in the form of grayscale images with value of each “pixel” in a slice ranging from 0 to 256. For the current data, the metal matrix has values at the higher end of the limit while voids have values towards the lower end. This data needs to be separated to extract all the pixels that belong to a void. Typically, in image processing, this is achieved by thresholding the image by a certain value. For example, all pixels with a value of 128 and more can be deemed matrix and pixel with a value below 128 a void. Using such generalized value assumes that each slice in the data set and all other specimens have similar thresholds that will give “realistic” volume fractions for voids. The observations from the CT data suggest that the threshold does indeed change from specimen to specimen if not within the same specimen. There are various thresholding algorithms that are recommended for image processing. To find the algorithm that works best for the CT scans, several different methods are tested on a few small regions that contained voids viz. global thresholding, Gaussian thresholding and OTSU thresholding. OTSU thresholding provided the best results. It works well on data sets which have binary distribution of data like the one measured by CT. Most pixels in the CT image belong to the matrix and have a higher value with a certain distribution while, the voids have lower value. In OTSU thresholding, the threshold value is calculated using the following procedure:

- First, the histogram of the pixel values is obtained.
- The threshold value is calculated as the value that clearly divides the two areas under the curves equally.

The added advantage of using OTSU threshold is that it is an adaptive approach. On each CT scan slice, the threshold is calculated by the algorithm. The threshold value might be quite different in each slice as well as across different specimens and can therefore provide a more correct calculation of the actual voids. The thresholding gives better results when paired with a certain image smoothing procedure. In this work, various blurs are used to smooth the images viz. no blur, median blur (with various aperture sizes), gaussian blur (with different kernel sizes) etc. The smoothing that worked best is median blur with an aperture size of 5 pixels.

This procedure identifies all the pixels in each slice that belongs to voids. However, all such pixels that form a contiguous volume need to be “collected” together to form voids. As the size and shape of the voids can be associated with the location and intensity of strain localization during deformation, it is very important to correctly obtain the distribution of these voids. In this work, the clustering of pixels into voids is done by using unsupervised learning. A wide variety of clustering techniques are available. K-means and X-means are centroid based methods that can be used for clustering. The preferred approach for this work is density based spatial clustering of applications with noise ‘DBSCAN’ ([Ester et al., 1996](#)). It works well for identifying clusters in a region of space with high density of points while ignoring points in relatively lower density/connectivity. This makes the DBSCAN ideally suited for the

application of contiguous volumes that form voids from individual pixels. This also ignores points that might be noise in the CT data. Once the clusters are identified, the moments of each cluster are used to calculate an average ellipsoid for each void. This procedure is used to calculate the shape and size of voids with respect to the pulling direction.

As mentioned in the previous section, the extracted DIC data is on a grid with the average spacing between each point being $50 \mu\text{m}$ (see Fig. 9). The void data calculated from CT measurements is on a finer scale, thus the CT data is to be averaged before its reconciliation with the DIC measurements. Additionally, the DIC data is only available for the specimen surface. However, the subsurface distribution of voids can also influence strain localization at the surface and needs to be accounted for. To this end, the following approach is proposed and employed in this work:

- Align the CT measurements with the DIC data.
- Using the center of each grid point in the DIC, create a box with length and width of $50 \mu\text{m}$ each and entire depth of the specimen.
- “Average” all the quantities of interest in the box viz. voids size, volume fraction and aspect ratio along the principal directions (i.e. laboratory axes).

This forms the raw data that is used for subsequent training using an ML method described in section 3.3.

3.2. Feature selection

A successful implementation of machine learning framework requires inherent knowledge of the system to be modeled. Although, prior understanding of the exact relationship between the input and output parameters of the system is not necessary, it is important to have enough understanding of the system to be able to identify the important governing parameters. In this respect, feature selection or engineering is performed to define the most representative and compact set of features for a given system. The material system under consideration in the present work is an additively manufactured aluminum alloy with complex microstructure (see Fig. 5), consisting of the process induced porosity and heterogeneous deformation characteristics. The process induced porosity is one of the key factors that influence localization and failure in these alloys (Laursen et al., 2020). It is acknowledged that other factors such as the local crystallographic texture, dislocation content and residual stresses would also affect the strain localization and failure during tensile loading. However, for simplicity, only the effects of the underlying porosity distribution on local strain evolution and failure are considered in the present study. The selected features of interest are outlined in Table 4 below.

3.3. ANN Model

The feed forward neural network (FFNN) with backpropagation is used in the present study. It is a supervised learning algorithm that maps a given set of inputs to outputs using a function $f : S^i \rightarrow S^o$, where i is the number of dimensions for input and o is the number of dimensions for output. The purpose of training is to learn the function f using the available training dataset. The function f is found by minimizing the cost function C , which is a measure of how well the neural network performs with respect to the network predicted output $f(x)$ and the target value y . The cost function C is calculated as an average of the individual losses over the entire dataset, as follows

$$C = \frac{1}{m} \sum_{i=1}^m L_i \quad (2)$$

where L_i represents the loss value for the i^{th} training sample and m is total number of training samples. Fig. 10 shows a schematic representation of an artificial neural network with a single hidden layer. The input layer consists of a set of neurons $\{x_i | x_1, x_2, x_3, \dots, x_n\}$ representing the input features and the output layer represents a single output $f(x)$. Each neuron in the hidden layer transforms the values of the previous layer using a weighted linear summation $w_1x_1 + w_2x_2 + \dots + w_nx_n$, followed by multiplication with a non-linear activation function ϕ . The output y of each neuron can be calculated as

Table 4
Selected features name and description.

Feature	Description
<i>Print Direction (P_d)</i>	Specimen print direction (i.e. X00, X90, Y00, Y90, XY90)
<i>Grid Location (G_l)</i>	Location of the region of interest on x,y grid within the gage section of the specimen
<i>Time (t)</i>	Time in seconds during tensile deformation of specimen
V_f	Average volume fraction of porosity within the region of interest
V_s	Average pore size within the region of interest
V_x	Pore size or elongation along the x-axis
V_y	Pore size or elongation along the y-axis (loading axis)
V_z	Pore size or elongation along the z-axis

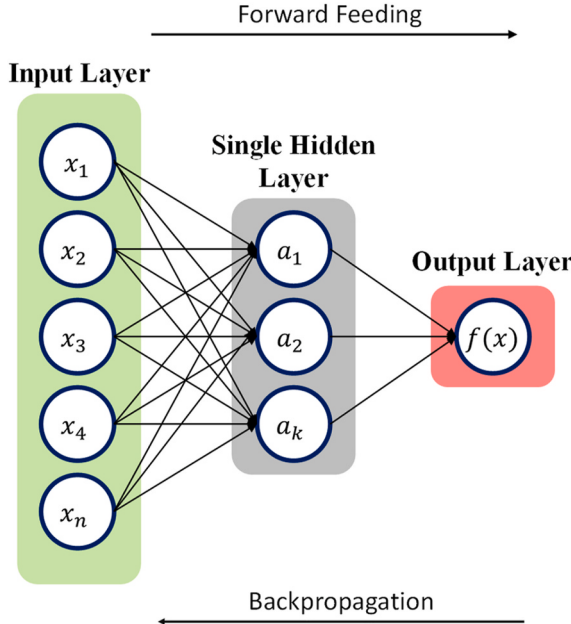


Fig. 10. Schematic representation of ANN with single hidden layer.

$$y = \phi \left(\sum_{i=1}^q w_i x_i + b_i \right) \quad (3)$$

where w_i and b_i represent the weight and bias of the i th input, and q is the number of elements in the input vector x . The output layer is connected to the last hidden layer and transforms its values to an output.

At the beginning of the first forward pass of ANN, the weights and biases are initialized, the inputs are fed into the network, and an initial prediction is made. The error function is computed, and a backpropagation algorithm is used to iteratively adjust the weights and biases to minimize the cost function. The backpropagation algorithm calculates how much the output values are affected by each of the weights in the model by calculating the partial derivative of the cost function C with respect to the weights w_{ij} , as follows

$$\frac{\partial C}{\partial w_{ij}^k} = \frac{\partial C}{\partial S_{NN}} \frac{\partial S_{NN}}{\partial w_{ij}^k} \quad (4)$$

where S_{NN} represents the network output and w_{ij}^k represents the weight for the connection from the j th neuron in the $(k-1)^{th}$ layer to the i^{th} neuron in the k^{th} layer of the network. The new weights $(w_{ij}^k)_{new}$ are computed using a stochastic gradient descent (SGD) scheme

$$(w_{ij}^k)_{new} = (w_{ij}^k)_{old} - \eta \frac{\partial C}{\partial w_{ij}^k} \quad (5)$$

where η is the learning rate and represents the step-size by which the weights are updated. In dense neural networks, a batch of input samples are run in one big forward pass and then the backpropagation is performed on the cumulative result to update the weights. More, details on the SGD and backpropagation algorithm can be found in Rumelhart et al. (1986). In this work, a mean-squared error function (MSE) is used for computing the losses and evaluating the training performance of the network. The error function E is written as

$$E = \frac{1}{m} \sum_{i=1}^m (y_i - f(x_i))^2 \quad (6)$$

where y_i is the actual value and $f(x_i)$ is the predicted value.

The activation function ϕ (in eq. (3)) determines the output of each neuron in the neural network. Some classical activation functions include sigmoid, ReLu and hyperbolic tangent functions. The current work employs the tanh function, given as

$$\phi(z) = \frac{e^z - e^{-z}}{e^z + e^{-z}} \quad (7)$$

The tanh function has a much stronger gradient than sigmoid function, which allows faster convergence and optimization of the network (LeCun et al., 2012). Apart from the choice of activation function, ANN are very sensitive to input data. Therefor, to avoid

suppressing the influence of smaller value from higher valued input variables, all data is normalized within the range [-1 1], in the present work. The normalized values x_n for each input value x_i are calculated as

$$x_n = \frac{2(x_i - x_{min})}{x_{max} - x_{min}} - 1 \quad (8)$$

where x_{max} and x_{min} are the maximum and minimum values within the raw input data.

The ANN training is performed using python and Keras with Tensor Flow backend. Prior to training, the dataset is split into training (70%) and testing (30%) datasets. The training dataset is further split and approx. 11% of it is used as validation set. The training dataset is used for training and learning of ANN, whereas the validation set is used to check the accuracy of the fitted parameters. The validation set provides an unbiased evaluation of a model fit on the training dataset during the fitting process and prevents the network from overfitting the data (Schmidhuber (2015)). The test dataset is previously unseen by the network and is used to evaluate the predictive capability of the final trained ANN model. The network weights are initialized randomly using the ‘glorot uniform’ kernel and Adams algorithm is used for adaptive learning rate optimization. The algorithm is designed specifically for training deep neural networks to achieve faster optimized results (Goodfellow et al., 2016).

3.4. Network architecture

Inputs to the ANN are the tensile test and porosity related parameters and the outputs are the local strain distribution values. Specifically, the inputs consist of specimen *Print Direction* (P_d), *Grid Location* (G_l) which represents the location of the region of interest within the gage section of tensile specimen, *Time* (t) during tensile deformation, V_f volume fraction of porosity, V_s size of pores, V_x , V_y , and V_z which correspond to the size of pores along the x , y and z axis within the region of interest. Each input data sample is represented by an array (P_d , G_l , t , V_f , V_s , V_x , V_y , V_z). Similarly, the outputs of the network are represented by an array (ϵ_{xx} , ϵ_{yy}), where ϵ_{xx} is the local strain in width direction and ϵ_{yy} is the local strain along the axial loading direction. The total number of samples within the training and validation datasets are approx. 183,320,928 and 20,368,992, respectively. It is noted that only time (t) is used as a descriptor for the current state of plastic deformation. Other descriptors such as strain rate could be employed as it is a more fundamental descriptor of plastic deformation. However, in current study, all experiments were conducted at a single applied strain rate, hence it was not used as an input. Nevertheless, the proposed framework can be easily extended to incorporate strain rate effects.

A grid search approach is employed to train few networks using different hyperparameters and the best performing network is selected. The effects of the total number of layers, the number of neurons per layer and the choice of activation functions on the performance of the network are studied. Fig. 11 shows the evolution of mean squared error (MSE) for the training and validation datasets corresponding to the different network architectures. The legend in the figure shows the number of layers and the corresponding number of neurons within each layer of the network. It is observed that the error decreases significantly by several orders of magnitude as the number of layers are increased from 1 to 4. The error decreases further by an order of magnitude, from 10^{-4} to 10^{-5} , as the number of layers are increased from 4 to 6. Further increase of the number of layers, from 6 to 8, reduces the MSE by a factor of five, at the cost of increasing complexity. Any further increase in the number of layers would not improve the MSE by a noticeable amount but will significantly increase the complexity of the network. It is also observed that the gradual decrease of the number of neurons for each subsequent layer following the 1st layer helps in reducing the complexity of the model.

The effects of the choice of activation function on network performance are also investigated. For this purpose, the network with 8 hidden layers is selected, the training is performed using rectified linear unit (ReLU), sigmoid and tanh activation functions and the results are presented in Fig. 12. These are the commonly used activation functions for ANN regression problems. It can be observed that

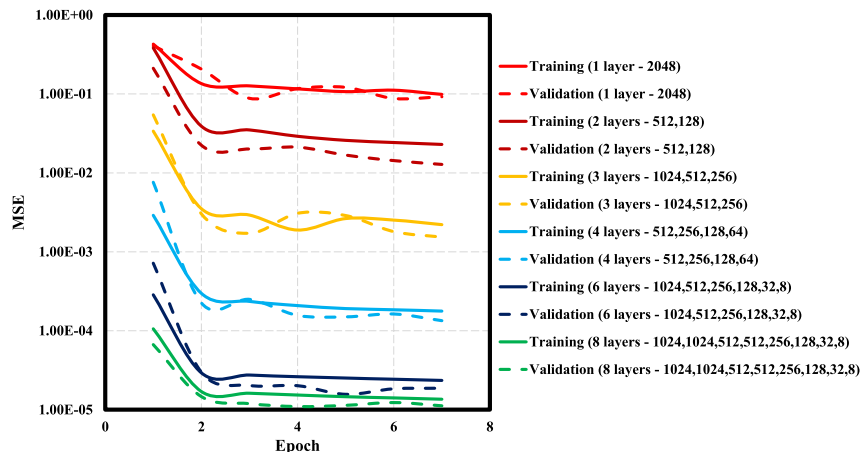


Fig. 11. Neural network learning curves showing the evolution of losses for training and validation datasets. The legend in the graph represents the different network architectures (number of layers – number of neurons per layer).

the MSE is highest for ReLU activation function which suggests that the network is unable to capture the inherent non-linearity and complexity of the problem. On the other hand, the MSE for tanh function is two orders of magnitude lower than that for ReLU activation function and an order of magnitude lower than that for sigmoid activation function. Based on these results, the network with 8 hidden layers and tanh as activation function is used for further analysis.

Fig. 13 shows a schematic representation of the proposed ANN architecture. The network consists of 8 inputs, 8 hidden layers and 2 outputs. The first two hidden layers have 1024 neurons each, the next two hidden layers have 512 neurons each, the next four layers have 256, 128, 32 and 8 neurons, respectively. Since, the neural network is deep with large amount of input data, a batch size based approach is used to feed data for training. At the beginning of each epoch, the training data is randomly split into batches of 8192 data samples and each batch is then sequentially fed to the network. The training for ANN is performed over 30 epochs. **Fig. 14** shows the evolution of losses (as mean squared error) for the training and validation datasets after each epoch. It is noticed that both the training and validation losses decreased to a point of stability with a minimal gap between them, indicating a possible generalization of the neural network model.

4. Results and discussion

4.1. Combined CT and DIC results

As discussed previously, the computed tomography and digital image correlation data are coupled to study the evolution of local strain with respect to the underlying porosity within the gage section of tensile specimens. Accordingly, **Fig. 15** shows a comparison of the local strain ε_y at failure and the initial distribution of pores within the gage section of X00 (**Fig. 15(a and b)**), Y00 (**Fig. 15(c and d)**), X90 (**Fig. 15(e and f)**), Y90 (**Fig. 15(g and h)**) and XY90 (**Fig. 15(i and j)**) tensile specimens. The specimens are pulled along the 'Y' direction. The build direction (BD) for the specimens is also indicated in **Fig. 15**. The color of the circles in **Fig. 15** represents the local strain value and their size represents the relative volume of porosity at that grid location. It is observed that the volume of pores and their distribution is different across specimens. Specifically, X90_1, Y90_2 specimens show lower porosity compared to other specimens. It is also interesting to note that for several specimens, the location of failure (i.e. dark red circles with relatively higher strain) corresponds to the location with high volume of pores (i.e. see arrows in **Fig. 15** pointing at regions with higher density of circles or bigger size circles). This is especially true for X00_1, Y00_2, X90_2 and XY90_2 specimens. The average void size and volume fraction of voids within each specimen is given in **Table 5**. It is noted that the average void size ranges from 26 μm for X90_1 to 31 μm for X00_1 and Y00_1 specimens. It is noted that X00_1 specimen has the highest volume fraction of porosity (see **Table 5**) and accordingly it has the lowest elongation to failure as shown in **Fig. 6**. Similarly, the volume fraction of voids within Y00_2 specimen (i.e. 0.022%) is higher as compared to Y00_1 specimen (i.e. 0.01%), and accordingly the elongation to failure for Y00_2 specimen (i.e. 12.2%) is comparatively lower than that for Y00_1 specimen (15.52%). This highlights the role and significance of porosity in influencing the local strain evolution and failure of AlSi10Mg specimens produced by SLM.

Fig. 16 and **Fig. 17** show a comparison of pore shape elongation along the x and y axis for the different tensile specimens. V_x represents the size of pores along the width direction and V_y represents the corresponding size along the loading direction of tensile specimen. At first glance, it can be observed that X00 and Y00 specimens (see **Fig. 16**) show a significant variation in the size of porosity as compared to X90, Y90 and XY90 specimens (see **Fig. 17**). Furthermore, there are several pores within X00 and Y00 specimens that are elongated along the x or y-axis. In addition, the overall pore size within X00 and Y00 specimens is larger as compared to X90, Y90 and XY90 specimens (see **Table 5**). These observations are consistent with elongation to failure results presented in **Fig. 6** and **Table 3**, where a comparatively lower ductility and larger variation in the total elongation to failure are observed for X00 and Y00 specimens. On the contrary, the X90 and Y90 specimens have more consistent smaller spherical pores (see **Fig. 17**), and consequently, the observed elongation to failure values for these specimens (in **Table 3**) are comparatively higher with relatively lower standard deviation. It is also noted that for X00_1 and Y00_1 specimens, the majority of larger pores are more elongated in the loading direction (i.e. $V_y > V_x$).

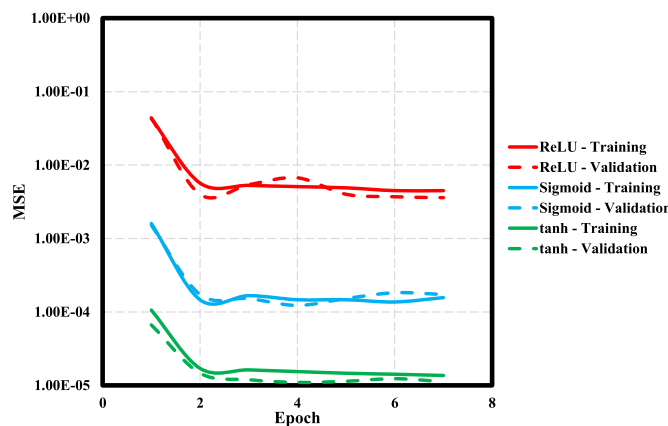


Fig. 12. Neural network learning curves showing the evolution of losses using different activation functions for training and validation datasets.

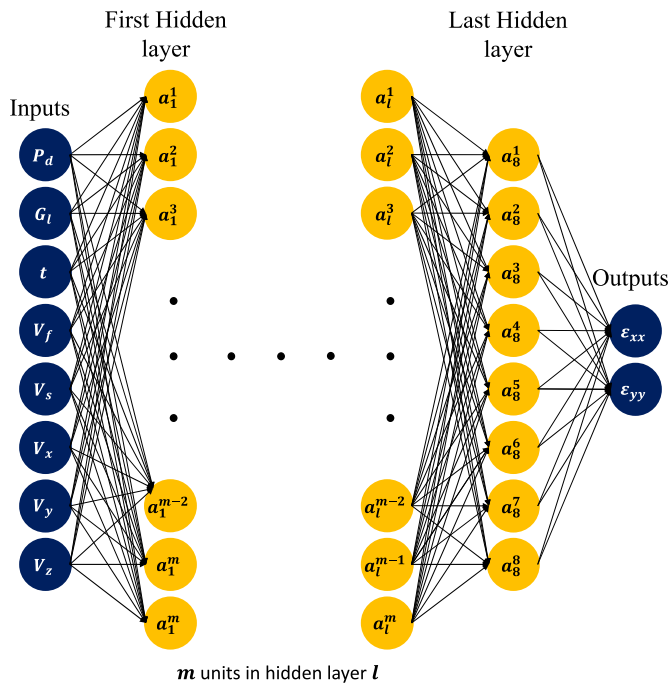


Fig. 13. Schematic of the proposed ANN architecture.

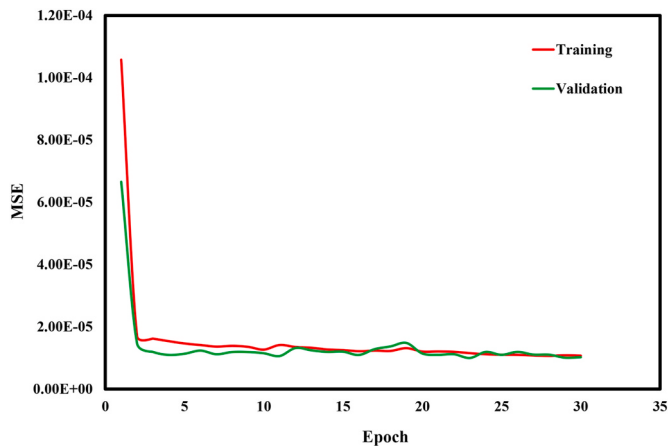


Fig. 14. Learning curve showing the evolution of losses for the training and validation dataset.

whereas the contrary is true for X00_2 and Y00_2 specimens. Hence, for specimen X00_1 and Y00_1, the tensile loading would promote closure of the already elongated pores resulting in relatively higher elongation to failure values observed for these specimens. On the contrary, larger pores in the X00_2 and Y00_2 specimens that are elongated along the width (i.e. x) direction would tend to open and coalesce more easily under tensile loading, thereby promoting early failure and lower elongation to failure values, as observed in Fig. 6. The results presented herein demonstrate a strong influence of the volume, size and shape of porosity on the local strain evolution and failure of AlSi10Mg alloy under tensile loading.

4.2. Artificial neural network results

Based on the experimental results, the relationship between the microstructure (i.e. porosity) and the mechanical performance of AlSi10Mg alloy is rather complex. In this regard, a successful implementation of an ANN model will enhance this understanding and would eventually help in development of a framework for predicting experimental trends in materials with complex heterogeneous microstructures. In the next few subsections, the ANN predictions for local strain distribution and plastic anisotropy evolution during tensile loading are compared and discussed in light of the corresponding experimental data.

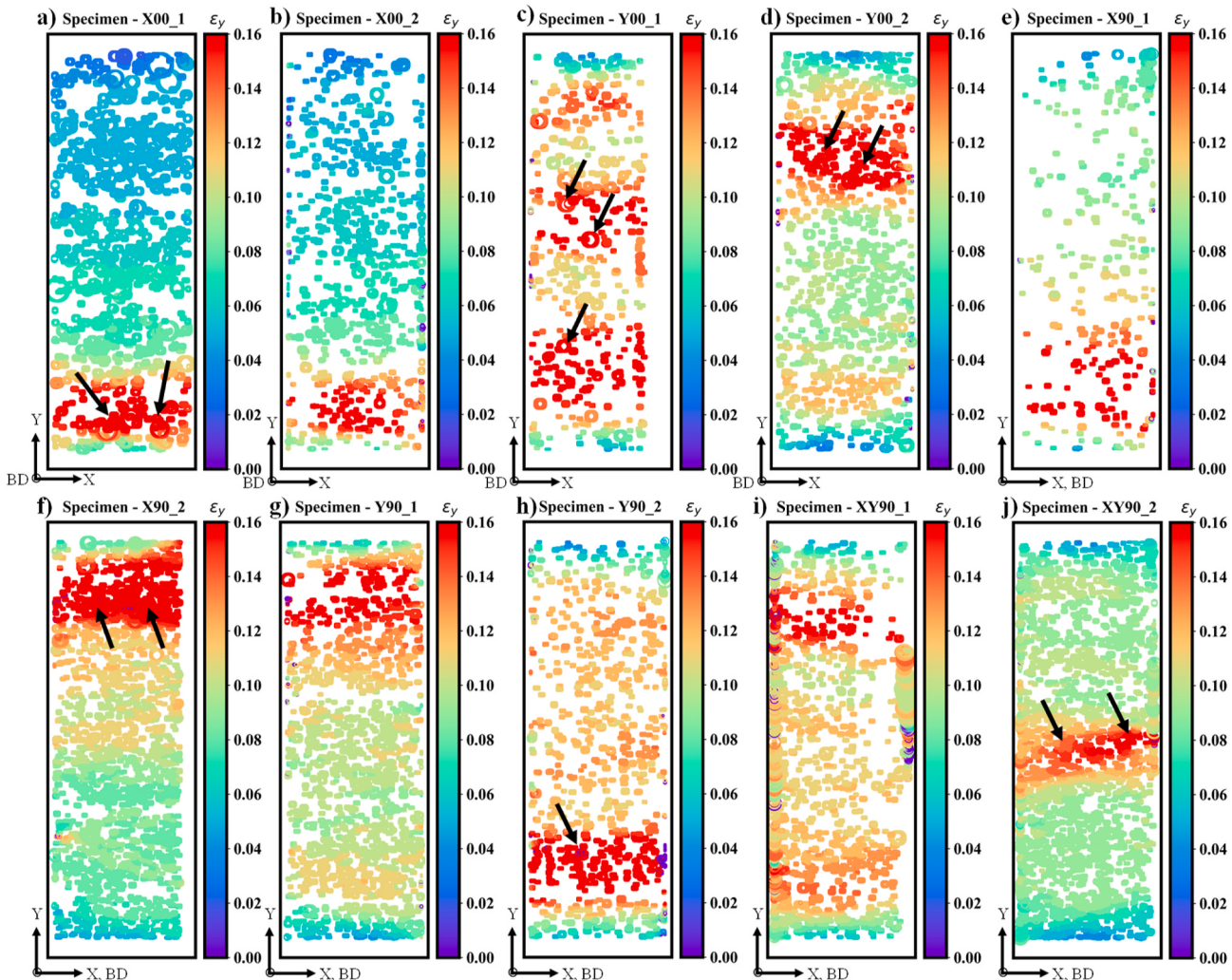


Fig. 15. Comparison between axial strain ε_y at failure and initial distribution of pores within the gage section of tensile specimens. Note: the size of circles represents the relative volume of porosity at that location and the color represents the corresponding local strain. (For interpretation of the references to color in this figure legend, the reader is referred to the Web version of this article.)

Table 5

Average void size and volume fraction (%) of voids within specimens.

Specimen	Average void size (mm)	Volume fraction of voids (%)
X00_1	0.031	0.09
X00_2	0.030	0.011
Y00_1	0.031	0.01
Y00_2	0.029	0.022
X90_1	0.026	0.006
X90_2	0.027	0.015
Y90_1	0.027	0.011
Y90_2	0.028	0.008
XY90_1	0.027	0.009
XY90_2	0.027	0.013

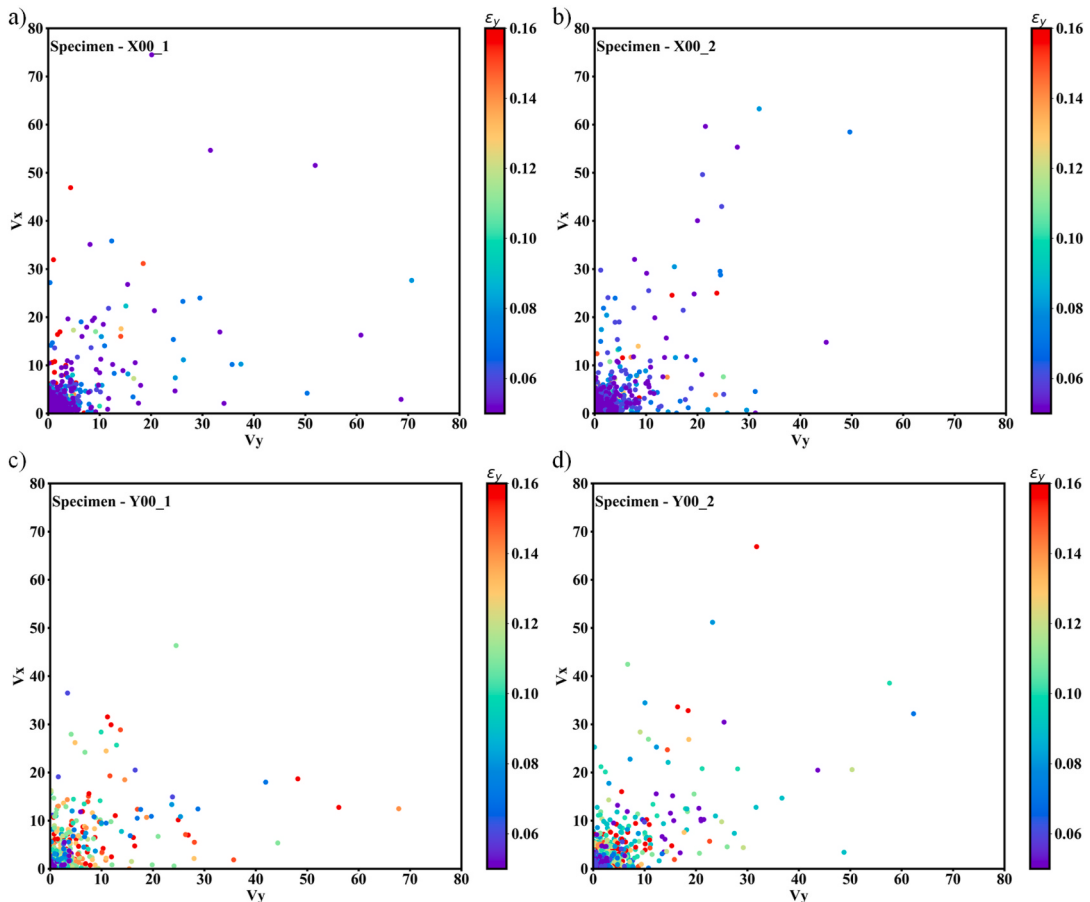


Fig. 16. Comparison of pore dimensions along the x and y axis in microns for X00 and Y00 specimens. Note: V_x represents the pore size in specimen width direction and V_y represents the corresponding size in longitudinal loading direction. The circle color represents the local strain ϵ_y at failure. (For interpretation of the references to color in this figure legend, the reader is referred to the Web version of this article.)

i. ANN predictions for local strain distribution

Fig. 18 and Fig. 19 show a comparison of ANN predicted local strain distribution ϵ_y within gage section at 4% and 8% global tensile strain and corresponding experimental data for X00, Y00, X90, Y90 and XY90 specimens. The corresponding MSE values are listed in Table 6. It can be observed that the ANN model shows excellent predictions for the local strain distribution during tensile loading of AlSi10Mg specimens. The model is able to predict the very early localization hotspots at 4% global strain for X00_1 and X00_2 tensile specimens (see encircled regions in Fig. 18(a and b)). At 4% strain, the tensile deformation is comparatively homogeneous across the gage section for X90, Y90 and XY90 specimens (see Fig. 19), and the ANN model successfully predicts that uniform strain distribution. The MSE for ANN predictions at 4% global tensile strain is negligible and is in the order of 10^{-6} across all specimens. It is observed that

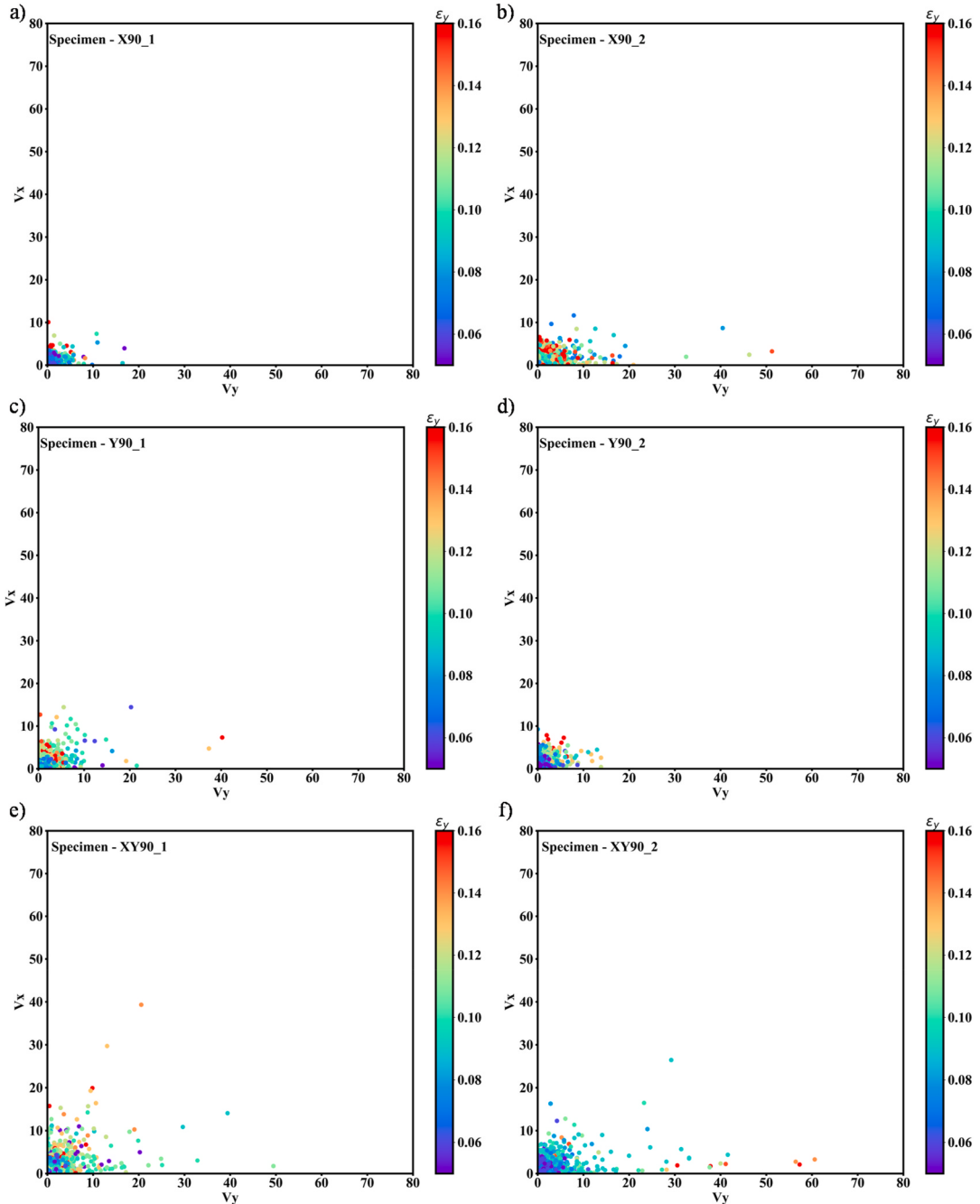


Fig. 17. Comparison of pore dimensions along the x and y axis in microns for X90, Y90 and XY90 specimens. Note: V_x represents the pore size in specimen width direction and V_y represents corresponding size in longitudinal loading direction. The circle color represents the local strain ϵ_y at failure. (For interpretation of the references to color in this figure legend, the reader is referred to the Web version of this article.)

strain has started to localize within the gage region of X00_1 and X00_2 specimens at 8% global deformation. This intense localized banding behavior and its location (near the bottom edge of the specimen) is correctly predicted by the ANN model. Similarly, the Y00_1 and Y00_2 specimens show presence of multiple strain hotspots within the gage region at 8% strain, which are also predicted properly by the proposed model. Furthermore, the model also predicts the local strain evolution and location of hotspots for X90, Y90 and XY90 specimens at 8% global strain (see Fig. 19). However, it is noticed that some of the very fine local fluctuations within the gage section are not fully captured. For instance, see the encircled region in Fig. 19(e), where the experimental results show some very fine scale local fluctuations (i.e. represented by local deviations in color) that are predicted in an average manner by the ANN model. Nevertheless, the model successfully captures all important aspects of tensile deformation, which is also reflected by the very low MSE values

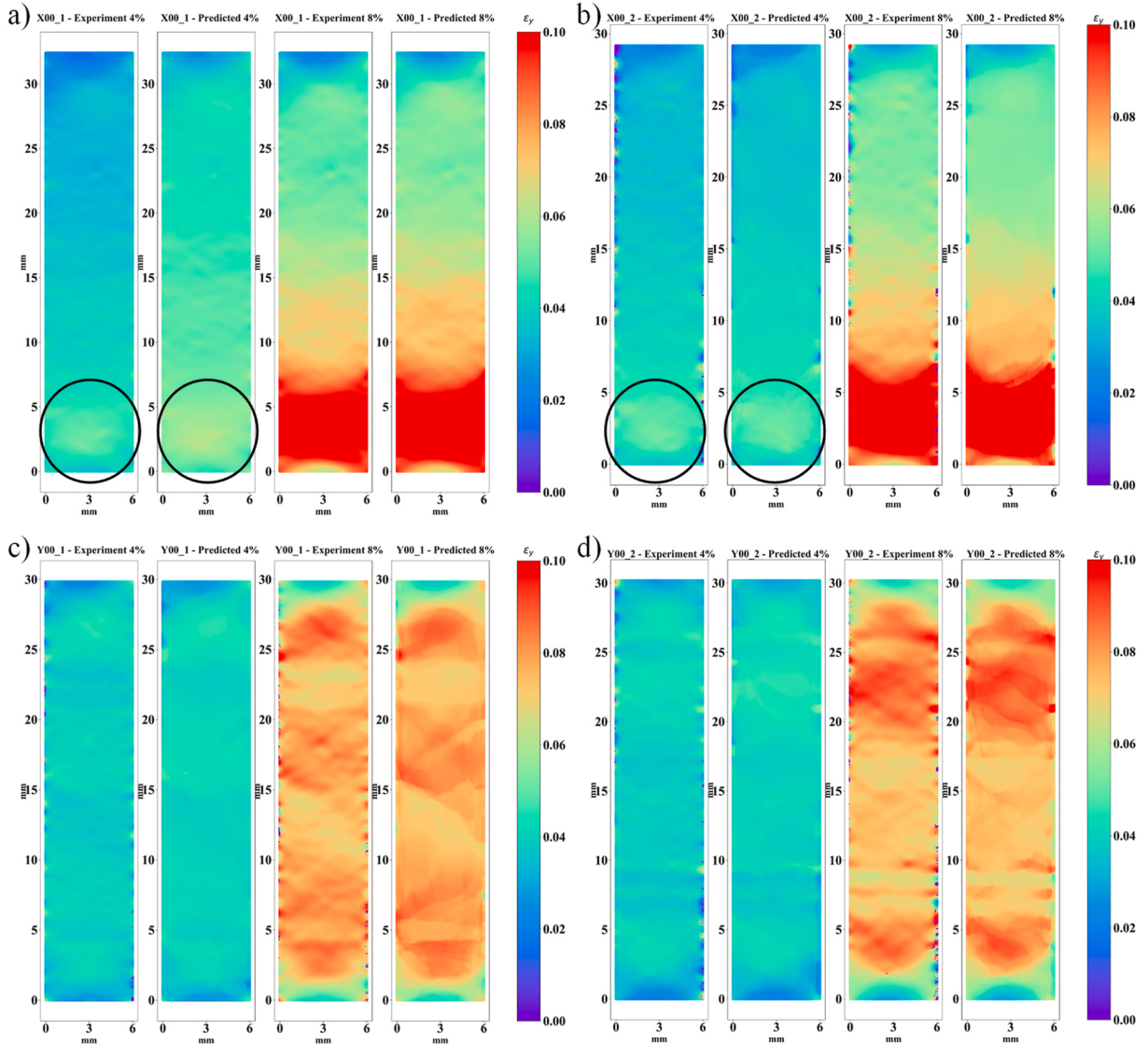


Fig. 18. Comparison of ANN predicted local strain distribution ε_y within gage section at 4% and 8% global tensile strain and corresponding experimental data for (a) X00_1, (b) X00_2, (c) Y00_1, and (d) Y00_2 specimens.

in the order of 10^{-5} (see Table 6).

ii. ANN predictions for fracture

The comparison of ANN predictions with corresponding experimental data for minor ε_x and major ε_y tensile strain distributions at failure are shown in Fig. 20 (for X00 and Y00) and Fig. 21 (for X90, Y90, XY90 specimens). The corresponding MSE values are given in Table 7. It is noted that the ANN model successfully predicts both the major and minor strain evolutions at failure across all specimens. This is also reflected by the low MSE values (see Table 7), which are in the order of $10^{-4} - 10^{-5}$. The proposed model also successfully captures the experimentally observed shear banding and localization behavior prior to failure. It is worth noting that the shape of the bands and the localization intensity are also well captured. Furthermore, the model also successfully predicts the location of crack initiation during tensile failure. This can be easily verified for specimens where the fracture process initiated near one of the edges. For instance, see the regions pointed at by arrows for X00_2, Y00_1, Y00_2 and XY90_2 specimens. It is noted that the MSE has been increasing from 4% to 8% deformation and failure. Nevertheless, the errors are rather negligible to cause any significant deviation from the observed experimental behavior.

ii. ANN predictions for plastic anisotropy evolution

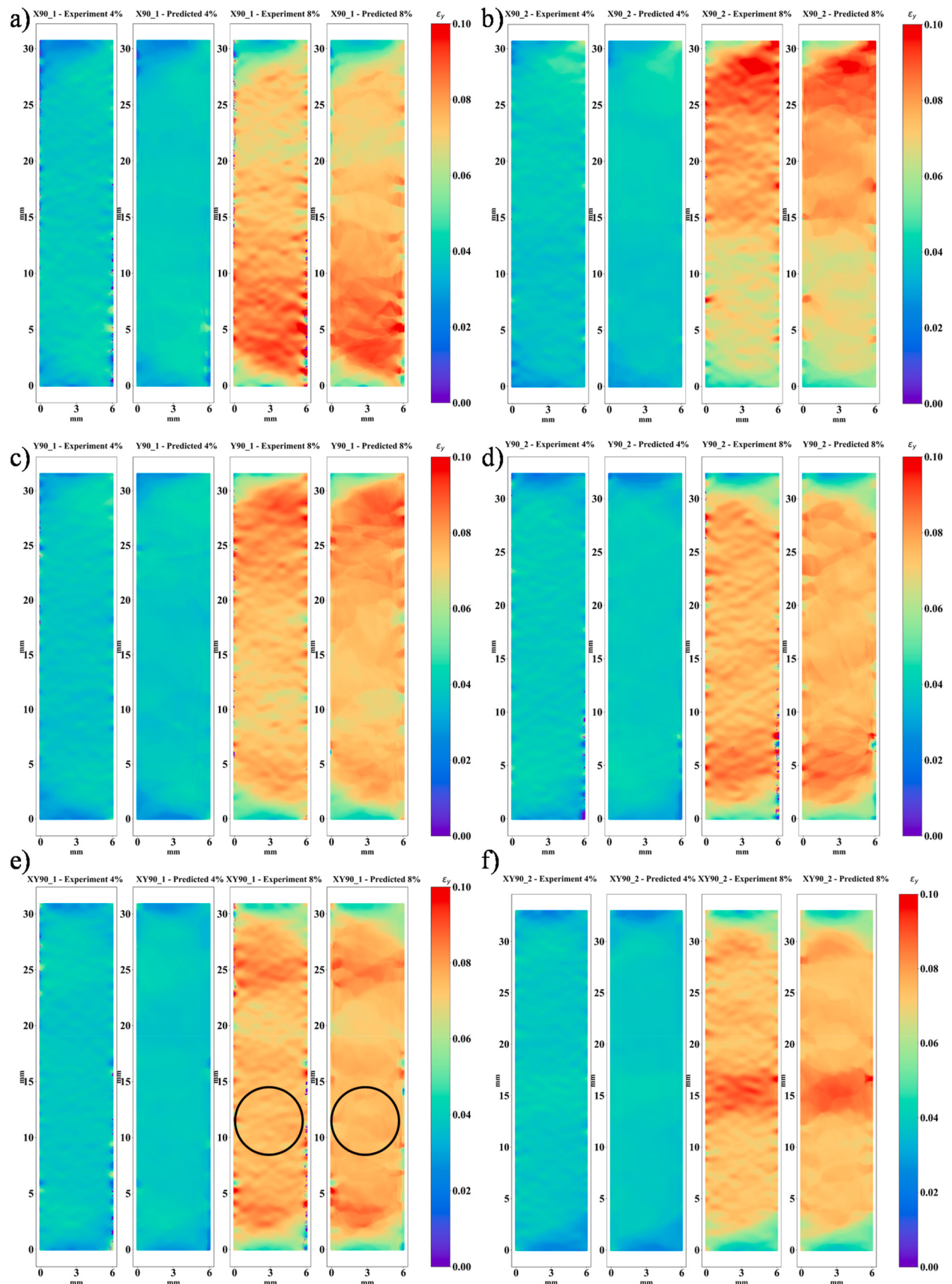


Fig. 19. Comparison of ANN predicted local strain distribution ϵ_y within gage section at 4% and 8% global tensile strain and corresponding experimental data for (a) X90_1, (b) X90_2, (c) Y90_1, (d) Y90_2, (e) XY90_1 and (f) XY90_2 specimens.

Fig. 22 and Fig. 23 show the comparison between experimental r-value evolution and ANN predictions at three different locations (i.e. Location-1 (R1): 1/4th - top, Location-2 (R2): 1/2 - center, and Location-3 (R3): 3/4th - bottom) along the gage length of X00, Y00, X90, Y90 and XY90 specimens. The r-values are computed using the DIC based point method (See Kang and Muhammad (2017) for more details). It is noted that the experimental r-value results show a similar evolution for X00 and Y00 specimens, which is different from the behavior exhibited by X90, Y90 and XY90 specimens. The r-value for X00 and Y00 specimens show an increase with plastic deformation, suggesting that more plastic strain is accommodated by deformation in the width direction of the tensile specimen. On the contrary, the r-value for X90, Y90 and XY90 specimens show a slight decrease with plastic deformation, suggesting that more deformation is accommodated by the thickness strain with persistent tensile deformation. These experimental results can have significant implications for formability of the alloy, where local thinning can cause premature failure.

It is observed that the ANN predicted r-value evolution across all specimens is in good agreement with the corresponding experimental data. The mean squared errors reported in Table 8 are in the order of $10^{-2} - 10^{-1}$. Since the r-values are calculated using DIC based point method, the results represent strain evolution at a very local scale within the gage section of tensile specimens. The ability of the proposed ANN model to be able to predict strain evolution at such scale is very promising. The results presented herein, suggest that an ANN based ML approach can be successfully applied to predict microstructure – property – performance relationships in materials with complex heterogeneous microstructures such as additively manufactured materials.

iv. Remarks regarding the value-added by current ANN approach

Additive manufacturing is a relatively new technology and the up-front costs of machine setup and printing of specimens is very expensive. The costs of conducting experiments and time requirements are also high. Furthermore, the microstructure produced by additive methods such as SLM are heterogeneous in nature with complex grain morphologies, texture gradient (as observed in Fig. 5), porosity, roughness and residual stresses. This leads to anisotropic material properties (such as directional anisotropy in stress-strain response as shown in Fig. 6 and r-values evolution as shown in Figs. 22 and 23) that are hard to evaluate and can significantly affect part performance in service. The main benefit of the application of ANN based machine learning algorithms lies in the fact that estimates of material property and performance are based purely on data and not on preconceptions, and that the ANN algorithms can establish linkages between different process and material related factors by learning trends and patterns within the available training dataset.

The current ML framework provides a numerical approach for prediction of important plasticity parameters such as local strain evolution, strain localization, r-value, and failure during tensile loading, based on non-destructive CT data. Once fully developed, the proposed approach would not require printing of costly test coupons or machining of test coupons from actual parts and would also save time and cost for experimentations. Furthermore, the proposed ANN approach with further extension may be applied to predict internal surface strain evolution for shapes such as hollow channels (i.e. characteristic of AM applications) where DIC strain measurements are impossible to be made along the inner wall. The success of the present approach motivates further use of ANN based ML techniques, as a powerful tool for material property assessment and accelerated development of new alloys, AM process optimization and its wide scale applicability.

5. Summary and conclusions

In the present work, a machine learning based framework is proposed to predict the evolution of local strains, plastic anisotropy and fracture during tensile deformation of an aluminum alloy AlSi10Mg fabricated by SLM. The proposed framework couples the methods and procedures involved in additive manufacturing and artificial intelligence to enable prediction of local strain heterogeneities that are observed during plastic deformation of AM materials. The framework includes printing of test specimens using LPBF technology, EBSD measurements to characterize the microstructure, micro-CT scanning to measure internal porosity distribution, mechanical testing using DIC to obtain local strain evolution, extraction and coupling of CT and DIC data, feature engineering to select

Table 6
Mean squared errors for local strain distribution ϵ_y predictions using ANN model.

Specimen	MSE at 4% Axial Strain	MSE at 8% Axial Strain
X00_1	$7.19 \cdot 10^{-6}$	$3.06 \cdot 10^{-5}$
X00_2	$9.33 \cdot 10^{-6}$	$2.01 \cdot 10^{-5}$
Y00_1	$5.37 \cdot 10^{-6}$	$1.17 \cdot 10^{-5}$
Y00_2	$6.88 \cdot 10^{-6}$	$1.92 \cdot 10^{-5}$
X90_1	$6.07 \cdot 10^{-6}$	$2.02 \cdot 10^{-5}$
X90_2	$1.79 \cdot 10^{-6}$	$6.80 \cdot 10^{-6}$
Y90_1	$2.81 \cdot 10^{-6}$	$8.12 \cdot 10^{-6}$
Y90_2	$3.55 \cdot 10^{-6}$	$1.37 \cdot 10^{-5}$
XY90_1	$4.70 \cdot 10^{-6}$	$1.21 \cdot 10^{-5}$
XY90_2	$1.35 \cdot 10^{-6}$	$3.31 \cdot 10^{-6}$

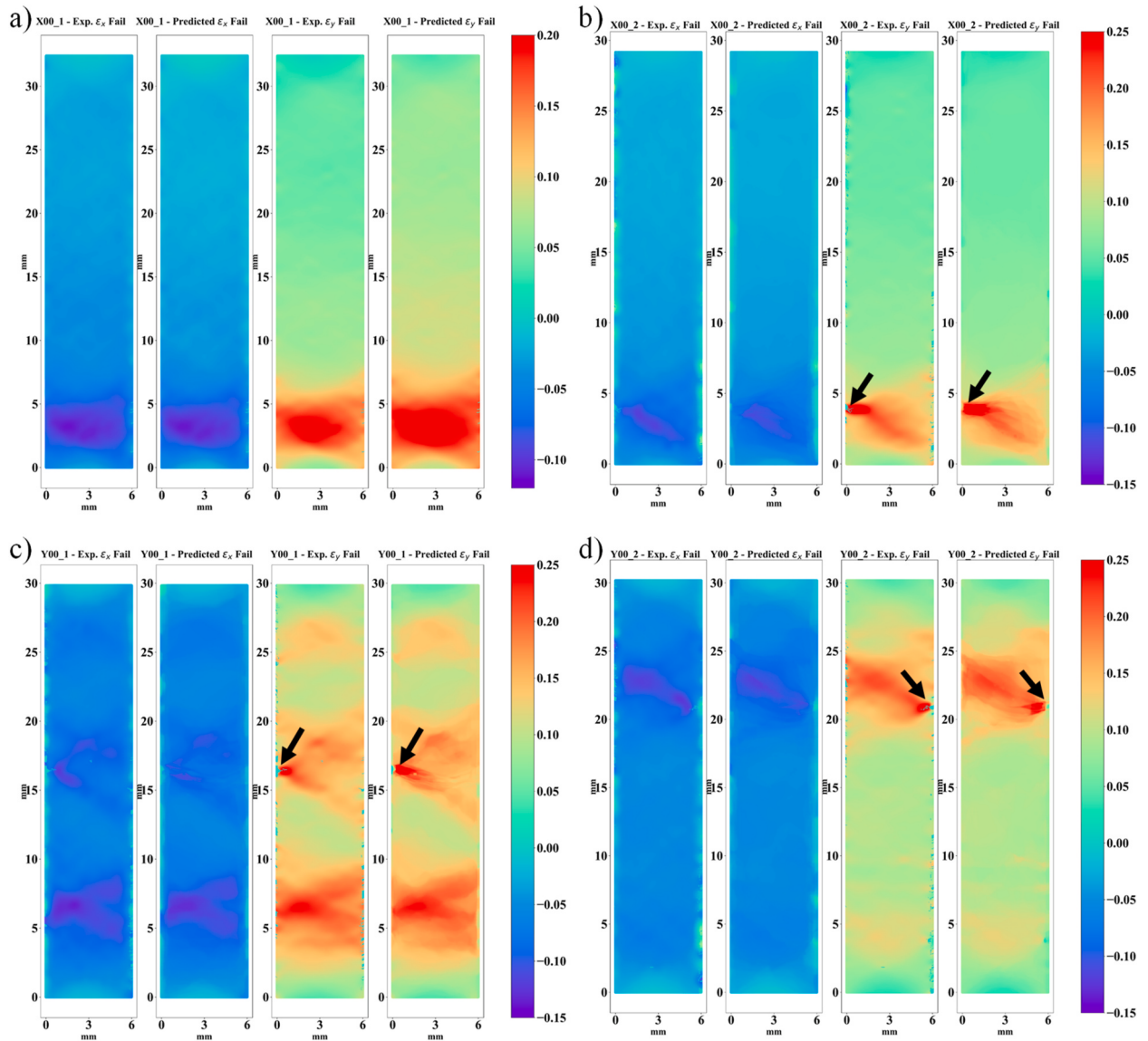


Fig. 20. Comparison of ANN predicted minor ε_x and major ε_y strain distributions at failure and corresponding experimental data for (a) X00_1, (b) X00_2, (c) Y00_1, and (d) Y00_2 specimens.

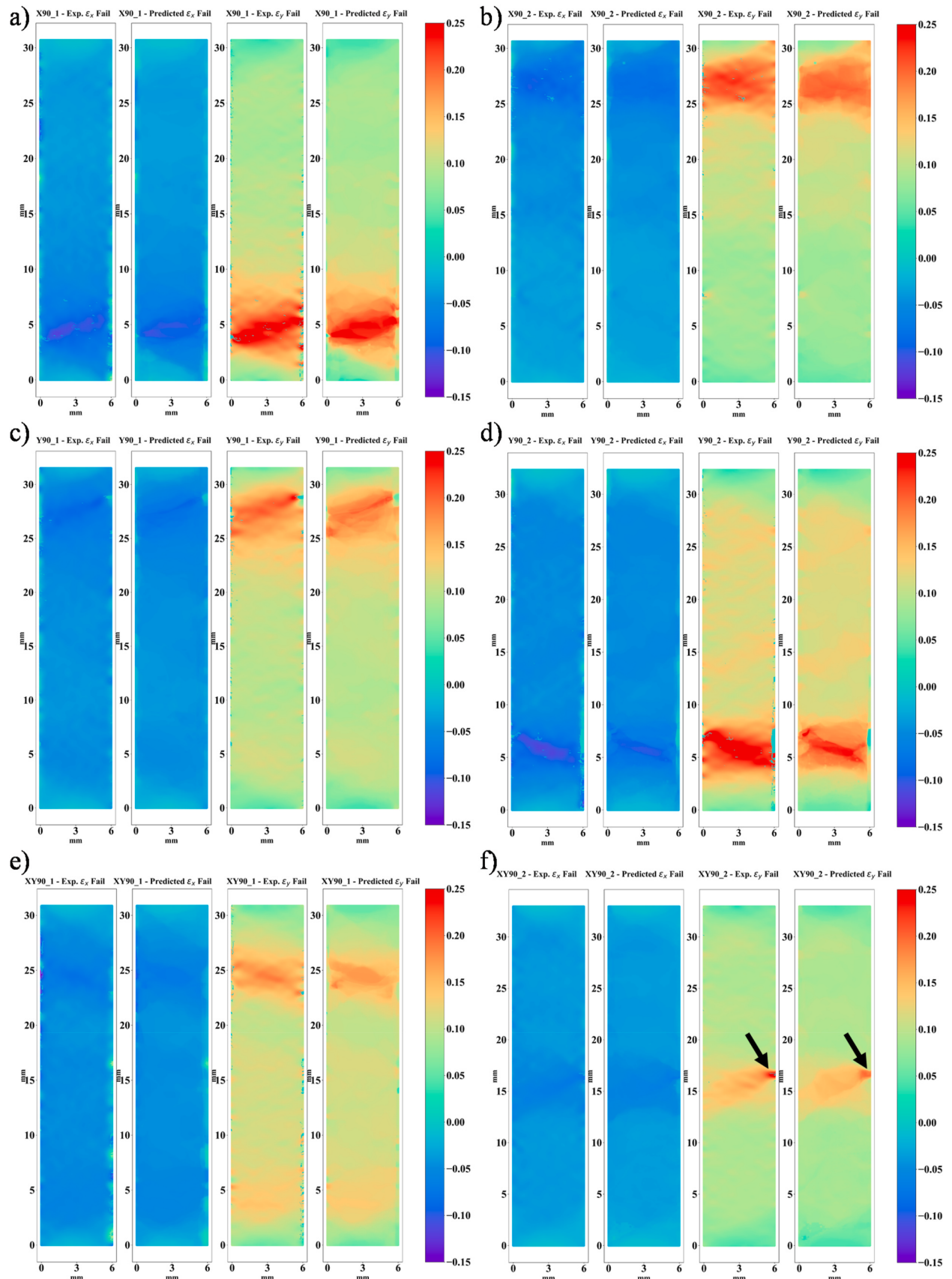


Fig. 21. Comparison of ANN predicted minor ϵ_x and major ϵ_y strain distributions at failure and corresponding experimental data for (a) X90_1, (b) X90_2, (c) Y90_1 (d) Y90_2, (e) XY90_1, and (f) XY90_2 specimens.

the most representative set of features and the development and evaluation of an artificial neural network model. The main goal of this work is to demonstrate the feasibility of ANN to predict local deformation response of materials with complex heterogeneous microstructures such as those produced by SLM. The current work predicts the evolution of local strains, plastic anisotropy and failure during plastic deformation of an additively manufactured material using machine learning techniques, such as ANN. Some important observations and conclusions are as follows:

- The microstructure of the AlSi10Mg specimens is complex in nature with considerable variation in the through thickness grain morphology, which changes as a function of the distance from the build plate. It is noted that the region closest to the build plate exhibits equiaxed grain morphology that gradually transitions into columnar morphology with increasing distance from base plate. Apart from the heterogeneity in grain shape, the through thickness texture also varies along the build direction. The columnar grains predominantly exhibit a near $<001>$ texture, whereas the $<101>$ and $<111>$ texture components are more apparent within equiaxed grains.
- It is noted that the average yield stress for X00 and Y00 specimens is approximately 10% higher than the X90, Y90 and XY90 specimens. Furthermore, a significant difference in ductility or elongation to failure is observed across all specimens. This difference is more pronounced for specimens with larger cross-sectional printing area per layer (i.e. X00 and Y00 specimens) and is associated with the size, shape and distribution of the underlying porosity. The lowest ductility is displayed by X00 specimens with an average elongation to failure of 9.3% whereas the highest ductility is shown by the Y90 specimens with an average elongation to failure of 13.7%.
- Unlike conventional metals, strain tends to localize across multiple regions within the gage section of the SLM printed AlSi10Mg alloy and the deformation is heterogeneous at the local scale, even at a very early stage of plastic deformation. It is noted that the plastic deformation is heterogeneous even at a relatively low axial strain of 4%.
- The average void size ranges from 26 μm for X90_1 to 31 μm for X00_1 and Y00_1 specimens. It is noted that the specimen with the highest volume fraction of porosity (i.e. X00_1 specimen with 0.09% of porosity) has the lowest elongation to failure of 8.53%. Similar behavior is observed for other specimens, where higher volume fraction of porosity led to lower tensile elongation to failure. Furthermore, the location of failure during tensile loading corresponds to the location with high volume of pores within the gage section of specimens. This emphasizes the role of porosity in influencing the local strain evolution and failure of AlSi10Mg specimens produced using SLM.
- The proposed ANN model consists of 8 inputs, 8 hidden layers and 2 outputs. Inputs to the ANN are the tensile test and porosity related parameters and the outputs are the local strain distribution values ϵ_x and ϵ_y . The network utilizes hyperbolic tangent as activation function within each layer. Adam algorithm is used for optimization of network weights and the training is performed over 30 epochs.
- The proposed ANN model successfully predicts the evolution of local strain heterogeneities during tensile deformation of AlSi10Mg alloy. The intensity and location of strain hotspots as well as the shape of shear banding behavior prior to failure are well captured. The mean squared error between the experimental and predicted strain values is in the range of 10^{-5} to 10^{-6} . The proposed model also successfully predicts the location of crack initiation during tensile failure. Furthermore, the model predictions for plastic anisotropy evolution are also in good agreement (i.e. MSE of 10^{-1} to 10^{-2}) with the corresponding experimental data. The ability of the proposed ANN model to successfully predict strain evolution at such local scale is very promising.
- One of the most important outcomes of the current work is a proof of feasibility: it is possible to build a machine learning based ANN framework in such a way that captures all the important characteristic features of plastic deformation and failure of engineering metals produced by SLM. The results presented herein, suggest that an ML based ANN approach can be successfully applied to predict microstructure – property – performance relationships in materials with complex heterogeneous microstructures such as additively manufactured materials.

Table 7
Mean squared errors for local strain distribution predictions at fracture using ANN model.

Specimen	MSE for ϵ_x at fracture	MSE for ϵ_y at fracture
X00_1	$3.69 \cdot 10^{-4}$	$4.66 \cdot 10^{-4}$
X00_2	$2.48 \cdot 10^{-5}$	$6.87 \cdot 10^{-5}$
Y00_1	$2.50 \cdot 10^{-5}$	$1.08 \cdot 10^{-4}$
Y00_2	$2.91 \cdot 10^{-5}$	$7.48 \cdot 10^{-5}$
X90_1	$4.82 \cdot 10^{-5}$	$2.33 \cdot 10^{-5}$
X90_2	$1.64 \cdot 10^{-5}$	$8.57 \cdot 10^{-5}$
Y90_1	$1.38 \cdot 10^{-5}$	$6.40 \cdot 10^{-5}$
Y90_2	$4.81 \cdot 10^{-5}$	$2.86 \cdot 10^{-4}$
XY90_1	$3.07 \cdot 10^{-5}$	$7.85 \cdot 10^{-5}$
XY90_2	$8.91 \cdot 10^{-6}$	$3.45 \cdot 10^{-5}$

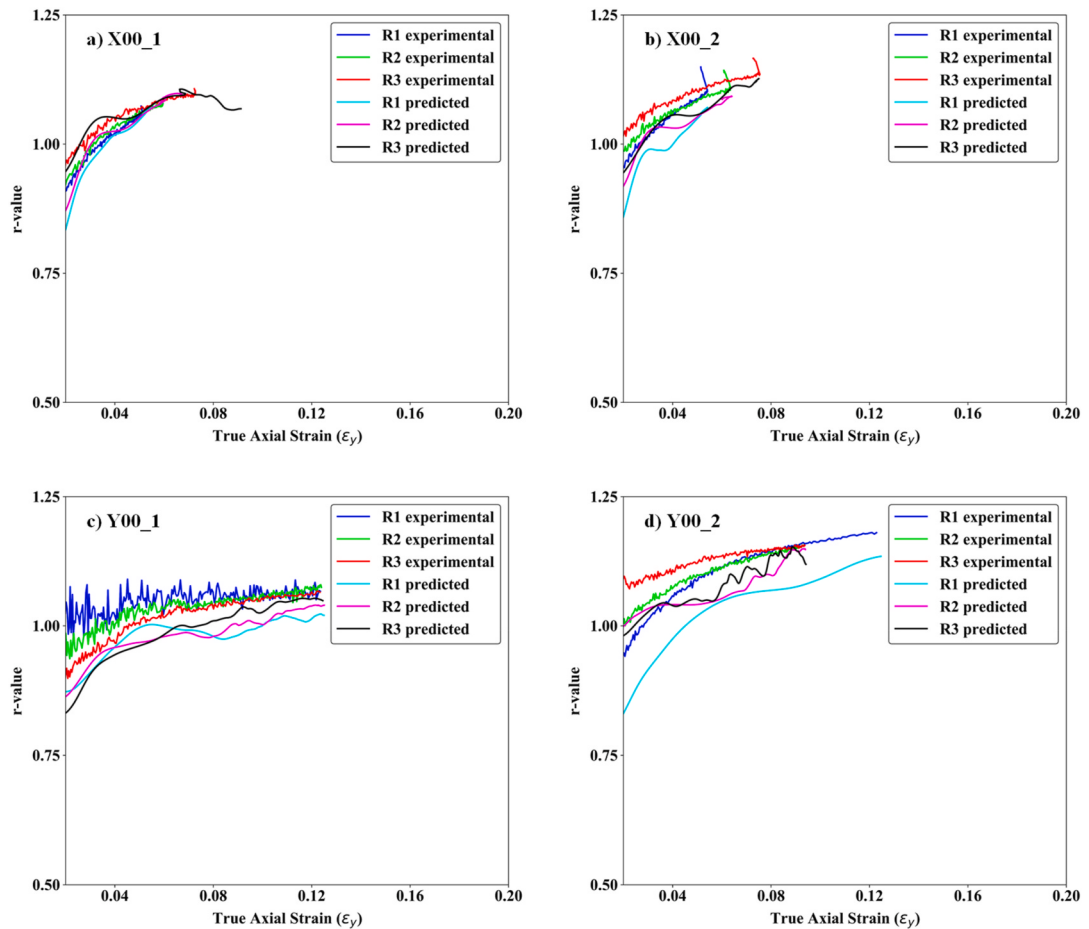


Fig. 22. Comparison of experimental r-value evolution with ANN predictions at location-1 (R1), location-2 (R2) and location-3 (R3) for (a) X00_1, (b) X00_2, (c) Y00_1, and (d) Y00_2 specimens.

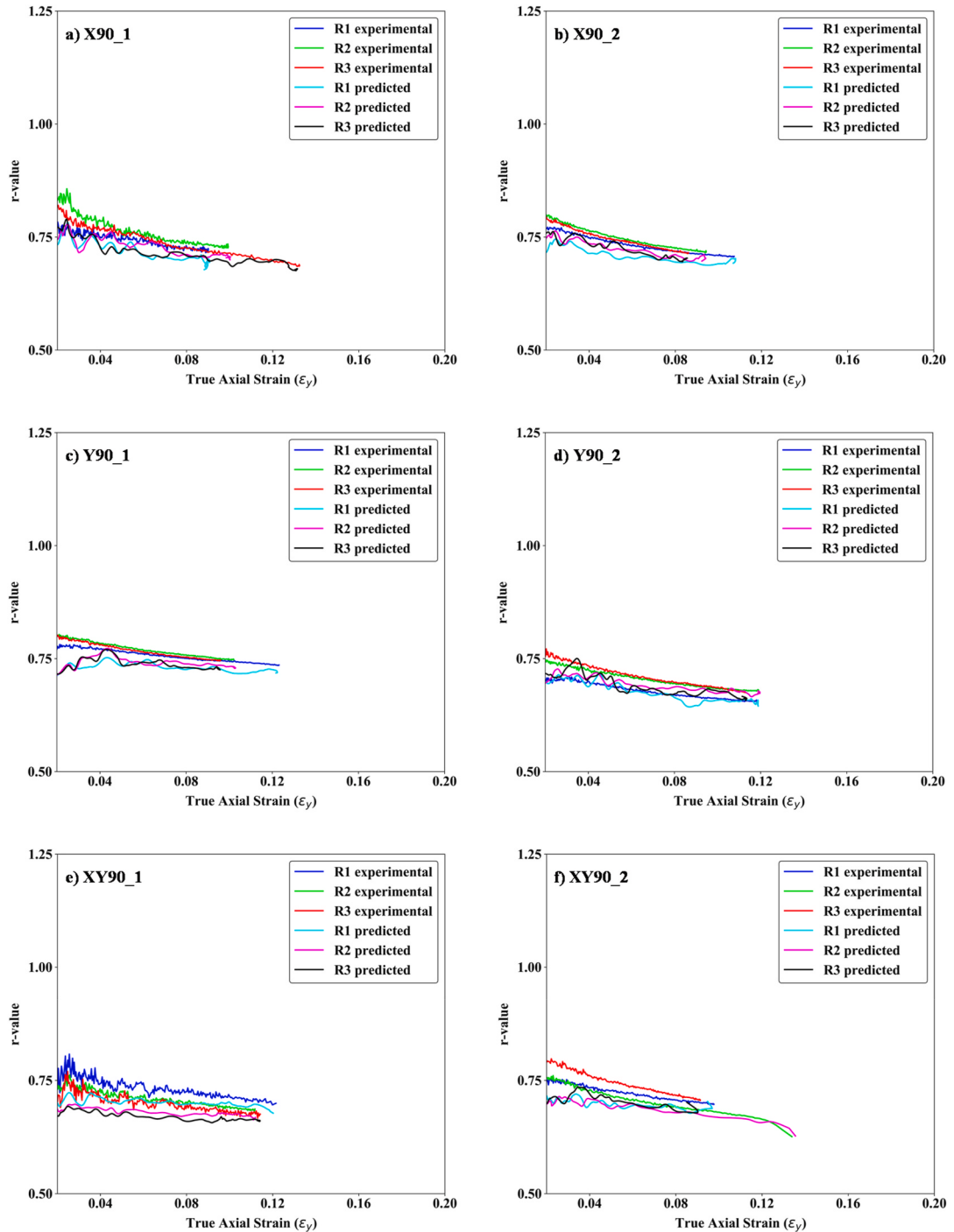


Fig. 23. Comparison of experimental r-value evolution with ANN predictions at location-1 (R1), location-2 (R2) and location-3 (R3) for (a) X90_1, (b) X90_2, (c) Y90_1, (d) Y90_2, (e) XY90_1, and (f) XY90_2 specimens.

Table 8
Mean squared errors for plastic anisotropy evolution predictions using ANN model.

Specimen	MSE for R1	MSE for R2	MSE for R3
X00_1	$2.11 \cdot 10^{-2}$	$3.91 \cdot 10^{-2}$	$2.38 \cdot 10^{-1}$
X00_2	$1.53 \cdot 10^{-2}$	$2.24 \cdot 10^{-2}$	$3.26 \cdot 10^{-2}$
Y00_1	$1.65 \cdot 10^{-0}$	$2.29 \cdot 10^{-1}$	$2.63 \cdot 10^{-0}$
Y00_2	$2.64 \cdot 10^{-2}$	$3.81 \cdot 10^{-2}$	$3.32 \cdot 10^{-0}$
X90_1	$5.42 \cdot 10^{-1}$	$9.66 \cdot 10^{-2}$	$1.00 \cdot 10^{-0}$
X90_2	$1.53 \cdot 10^{-2}$	$6.00 \cdot 10^{-1}$	$2.06 \cdot 10^{-1}$
Y90_1	$1.47 \cdot 10^{-2}$	$4.84 \cdot 10^{-2}$	$2.75 \cdot 10^{-1}$
Y90_2	$1.23 \cdot 10^{-2}$	$1.37 \cdot 10^{-2}$	$1.65 \cdot 10^{-2}$
XY90_1	$8.11 \cdot 10^{-2}$	$3.82 \cdot 10^{-2}$	$1.27 \cdot 10^{-1}$
XY90_2	$4.28 \cdot 10^{-1}$	$1.64 \cdot 10^{-2}$	$1.17 \cdot 10^{-1}$

CRediT authorship contribution statement

Waqas Muhammad: Conceptualization, Methodology, Investigation, Formal analysis, Visualization, Writing - original draft. **Abhijit P. Brahme:** Conceptualization, Methodology, Formal analysis, Writing - review & editing. **Olga Ibragimova:** Methodology, Formal analysis, Visualization. **Jidong Kang:** Investigation, Writing - review & editing, Supervision. **Kaan Inal:** Writing - review & editing, Supervision, Project administration, Funding acquisition.

Declaration of competing interest

The authors declare that they have no known competing financial interests or personal relationships that could have appeared to influence the work reported in this paper.

Acknowledgments

The authors are thankful to Natural Sciences and Engineering Research Council - Industrial Research Chair (NSERC-IRC) under grant no. IRCPJ-503185-2016, General Motors of Canada and CanmetMATERIALS of Natural Resources Canada for supporting this work.

References

- Ali, U., Esmaeilizadeh, R., Ahmed, F., Sarker, D., Muhammad, W., Keshavarzkermani, A., Mahmoodkhani, Y., Marzbanrad, E., Toyserkani, E., 2019a. Identification and characterization of spatter particles and their effect on surface roughness, density and mechanical response of 17-4 PH stainless steel laser powder-bed fusion parts. *Mater. Sci. Eng., A* 756, 98–107.
- Ali, U., Muhammad, W., Brahme, A., Skiba, O., Inal, K., 2019b. Application of artificial neural networks in micromechanics for polycrystalline metals. *Int. J. Plast.* 120, 205–219.
- Ali, U., Odoh, D., Muhammad, W., Brahme, A., Mishra, R.K., Wells, M., Inal, K., 2017. Experimental investigation and through process crystal plasticity-static recrystallization modeling of temperature and strain rate effects during hot compression of AA6063. *Mater. Sci. Eng., A* 700, 374–386.
- Asgari, H., Baxter, C., Hosseinkhani, K., Mohammadi, M., 2017. On microstructure and mechanical properties of additively manufactured AlSi10Mg_200C using recycled powder. *Mater. Sci. Eng., A* 707, 148–158.
- Bock, F.E., Aydin, R.C., Cyron, C.J., Huber, N., Kalidindi, S.R., Klusmann, B., 2019. A review of the application of machine learning and data mining approaches in continuum materials mechanics. *Front. Mater.* 6, 110.
- Bonatti, C., Mohr, D., 2017. Large deformation response of additively-manufactured FCC metamaterials: from octet truss lattices towards continuous shell mesostructures. *Int. J. Plast.* 92, 122–147.
- Brandl, E., Heckenberger, U., Holzinger, V., Buchbinder, D., 2012. Additive manufactured AlSi10Mg samples using Selective Laser Melting (SLM): microstructure, high cycle fatigue, and fracture behavior. *Mater. Des.* 34, 159–169.
- Bronkhorst, C.A., Mayeur, J.R., Livescu, V., Pokharel, R., Brown, D.W., Gray, G.T., 2019. Structural representation of additively manufactured 316L austenitic stainless steel. *Int. J. Plast.* 118, 70–86.
- Calignano, F., 2018. Investigation of the accuracy and roughness in the laser powder bed fusion process. *Virtual Phys. Prototyp.* 13, 97–104.
- Csanádi, T., Chinh, N.Q., Gubicza, J., Vörös, G., Langdon, T.G., 2014. Characterization of stress-strain relationships in Al over a wide range of testing temperatures. *Int. J. Plast.* 54, 178–192.
- Derogar, A., Djavanroodi, F., 2011. Artificial neural network modeling of forming limit diagram. *Mater. Manuf. Process.* 26, 1415–1422.
- Dobrzański, L.A., Honysz, R., 2009. Application of artificial neural networks in modelling of normalised structural steels mechanical properties. *J. Achiev. Mater. Manuf. Eng.* 32, 37–45.
- Elangovan, K., Sathiya Narayanan, C., Narayanasamy, R., 2010. Modelling of forming limit diagram of perforated commercial pure aluminium sheets using artificial neural network. *Comput. Mater. Sci.* 47, 1072–1078.
- Ester, M., Kriegel, H.-P., Sander, J., Xu, X., 1996. A density-based algorithm for discovering clusters in large spatial databases with noise. Proceedings of the Second International Conference on Knowledge Discovery and Data Mining, KDD'96. AAAI Press, pp. 226–231.
- Ferreri, N.C., Ghorbanpour, S., Bhowmik, S., Lussier, R., Bicknell, J., Patterson, B.M., Knezevic, M., 2019. Effects of build orientation and heat treatment on the evolution of microstructure and mechanical properties of alloy Mar-M-509 fabricated via laser powder bed fusion. *Int. J. Plast.* 121, 116–133.
- Flach, P., 2012. Machine Learning: the Art and Science of Algorithms that Make Sense of Data. Cambridge University Press.
- Gao, W., Zhang, Y., Ramanujan, D., Ramani, K., Chen, Y., Williams, C.B., Wang, C.C.L., Shin, Y.C., Zhang, S., Zavattieri, P.D., 2015. The status, challenges, and future of additive manufacturing in engineering. *CAD Comput. Aided Des.* 69, 65–89.
- Garibaldi, M., Ashcroft, I., Simonelli, M., Hague, R., 2016. Metallurgy of high-silicon steel parts produced using Selective Laser Melting. *Acta Mater.* 110, 207–216.
- Ghorbanpour, S., Alam, M.E., Ferreri, N.C., Kumar, A., McWilliams, B.A., Vogel, S.C., Bicknell, J., Beyerlein, I.J., Knezevic, M., 2020. Experimental characterization and crystal plasticity modeling of anisotropy, tension-compression asymmetry, and texture evolution of additively manufactured Inconel 718 at room and elevated temperatures. *Int. J. Plast.* 125, 63–79.

- Ghorbanpour, S., Zecevic, M., Kumar, A., Jahedi, M., Bicknell, J., Jorgensen, L., Beyerlein, I.J., Knezevic, M., 2017. A crystal plasticity model incorporating the effects of precipitates in superalloys: application to tensile, compressive, and cyclic deformation of Inconel 718. *Int. J. Plast.* 99, 162–185.
- Goodfellow, I., Bengio, Y., Courville, A., Bengio, Y., 2016. Deep Learning, vol. 1. MIT press, Cambridge.
- Grasso, M., Colosimo, B.M., 2017. Process defects and in situ monitoring methods in metal powder bed fusion: a review. *Meas. Sci. Technol.* 28, 1–25.
- Hadadzadeh, A., Amirkhiz, B.S., Li, J., Mohammadi, M., 2018. Columnar to equiaxed transition during direct metal laser sintering of AlSi10Mg alloy: effect of building direction. *Addit. Manuf.* 23, 121–131.
- Hadadzadeh, A., Shalchi Amirkhiz, B., Odeshi, A., Li, J., Mohammadi, M., 2019. Role of hierarchical microstructure of additively manufactured AlSi10Mg on dynamic loading behavior. *Addit. Manuf.* 28, 1–13.
- Hitzler, L., Janousch, C., Schanz, J., Merkel, M., Heine, B., Mack, F., Hall, W., Öchsner, A., 2017. Direction and location dependency of selective laser melted AlSi10Mg specimens. *J. Mater. Process. Technol.* 243, 48–61.
- Jenab, A., Sari Sarraf, I., Green, D.E., Rahmaan, T., Worswick, M.J., 2016. The Use of genetic algorithm and neural network to predict rate-dependent tensile flow behaviour of AA5182-sheets. *Mater. Des.* 94, 262–273.
- Kang, J., Muhammad, W., 2017. Measurement of plastic strain ratio using digital image correlation. *J. Test. Eval.* 45, 1587–1600.
- Kempen, K., Thijss, L., Humbeeck, Van, J., Kruth, J.P., 2015. Processing AlSi10Mg by selective laser melting: parameter optimisation and material characterisation. *Mater. Sci. Technol.* 31, 917–923.
- Kempen, K., Thijss, L., Van Humbeeck, J., Kruth, J.P., 2012. Mechanical properties of AlSi10Mg produced by selective laser melting. *Phys. Procedia* 39, 439–446.
- Khairallah, S.A., Anderson, A.T., Rubenchik, A., King, W.E., 2016. Laser powder-bed fusion additive manufacturing: physics of complex melt flow and formation mechanisms of pores, spatter, and denudation zones. *Acta Mater.* 108, 36–45.
- Khan, A.S., Liu, H., 2012. A new approach for ductile fracture prediction on Al 2024-T351 alloy. *Int. J. Plast.* 35, 1–12.
- Kiselyova, N.N., Gladun, V.P., Vashchenko, N.D., 1998. Computational materials design using artificial intelligence methods. *J. Alloys Compd.* 279 (1), 8–13.
- Kotkunde, N., Deole, A.D., Gupta, A.K., 2014. Prediction of forming limit diagram for Ti-6Al-4V alloy using artificial neural network. *Procedia Mater. Sci.* 6, 341–346.
- Ku, A.Y., Khan, A.S., Gnäupel-Herold, T., 2020. Quasi-static and dynamic response, and texture evolution of two overaged Al 7056 alloy plates in T761 and T721 tempers: experiments and modeling. *Int. J. Plast.* 130, 102679.
- Laursen, C.M., DeJong, S.A., Dickens, S., Exil, A.N., Susan, D.F., Carroll, J.D., 2020. Relationship between ductility and the porosity of additively manufactured AlSi10Mg. *Mater. Sci. Eng., A*, 139922.
- LeCun, Y., Bengio, Y., Hinton, G., 2015. Deep learning. *Nature* 521, 436–444.
- LeCun, Y.A., Bottou, L., Orr, Geneviève B., Müller, K.-R. (Eds.), Efficient BackProp BT - Neural Networks: Tricks of the Trade, second ed. Springer Berlin Heidelberg, Berlin, Heidelberg, pp. 9–48.
- Li, W., Li, S., Liu, J., Zhang, A., Zhou, Y., Wei, Q., Yan, C., Shi, Y., 2016. Effect of heat treatment on AlSi10Mg alloy fabricated by selective laser melting: microstructure evolution, mechanical properties and fracture mechanism. *Mater. Sci. Eng., A* 663, 116–125.
- Li, X., Roth, C.C., Mohr, D., 2019. Machine-learning based temperature- and rate-dependent plasticity model: application to analysis of fracture experiments on DP steel. *Int. J. Plast.* 118, 320–344.
- Li, Z., Voisin, T., McKeown, J.T., Ye, J., Braun, T., Kamath, C., King, W.E., Wang, Y.M., 2019. Tensile properties, strain rate sensitivity, and activation volume of additively manufactured 316L stainless steels. *Int. J. Plast.* 120, 395–410.
- Li, Zan, Li, Zhiqiang, Tan, Z., Xiong, D.-B., Guo, Q., 2020. Stress relaxation and the cellular structure-dependence of plastic deformation in additively manufactured AlSi10Mg alloys. *Int. J. Plast.* 127, 102640.
- Liu, J., To, A.C., 2017. Quantitative texture prediction of epitaxial columnar grains in additive manufacturing using selective laser melting. *Addit. Manuf.* 16, 58–64.
- Liu, J., Xiong, W., Behera, A., Thompson, S., To, A.C., 2017. Mean-field polycrystal plasticity modeling with grain size and shape effects for laser additive manufactured FCC metals. *Int. J. Solid Struct.* 112, 35–42.
- Liu, P.W., Wang, Z., Xiao, Y.H., Lebensohn, R.A., Liu, Y.C., Horstemeyer, M.F., Cui, X.Y., Chen, L., 2020. Integration of phase-field model and crystal plasticity for the prediction of process-structure-property relation of additively manufactured metallic materials. *Int. J. Plast.* 128, 102670.
- Liu, Y., Zhao, T., Ju, W., Shi, S., 2017. Materials discovery and design using machine learning. *J. Mater.* 3, 159–177.
- Liu, Y.J., Liu, Z., Jiang, Y., Wang, G.W., Yang, Y., Zhang, L.C., 2018. Gradient in microstructure and mechanical property of selective laser melted AlSi10Mg. *J. Alloys Compd.* 735, 1414–1421.
- Mangal, A., Holm, E.A., 2018. Applied machine learning to predict stress hotspots I: face centered cubic materials. *Int. J. Plast.* 111, 122–134.
- Muhammad, W., Brahma, A., Kang, J., Mishra, R., Inal, K., 2016. In: Williams, E. (Ed.), Large Strain Cyclic Simple Shear Behavior of Aluminum Extrusions: an Experimental and Numerical Study, Light Metals, pp. 169–174.
- Muhammad, W., Brahma, A.P., Ali, U., Hirsch, J., Engler, O., Aretz, H., Kang, J., Mishra, R.K., Inal, K., 2019a. Bendability enhancement of an age-hardenable aluminum alloy: Part II — multiscale numerical modeling of shear banding and fracture. *Mater. Sci. Eng., A* 754, 161–177.
- Muhammad, W., Sabat, R.K., Brahma, A.P., Kang, J., Mishra, R.K., Shalchi Amirkhiz, B., Hirsch, J., Inal, K., 2019b. Deformation banding in a precipitation hardened aluminum alloy during simple shear deformation. *Scripta Mater.* 162, 300–305.
- Olakanmi, E.O., Cochrane, R.F., Dalgarno, K.W., 2015. A review on selective laser sintering/melting (SLS/SLM) of aluminium alloy powders: processing, microstructure, and properties. *Prog. Mater. Sci.* 74, 401–477.
- Pokharel, R., Patra, A., Brown, D.W., Clausen, B., Vogel, S.C., Gray, G.T., 2019. An analysis of phase stresses in additively manufactured 304L stainless steel using neutron diffraction measurements and crystal plasticity finite element simulations. *Int. J. Plast.* 121, 201–217.
- Qin, Y.J., Pan, Q.L., He, Y.B., Li, W.B., Liu, X.Y., Fan, X., 2010. Artificial neural network modeling to evaluate and predict the deformation behavior of zk60 magnesium alloy during hot compression. *Mater. Manuf. Process.* 25, 539–545.
- Read, N., Wang, W., Essa, K., Attallah, M.M., 2015. Selective laser melting of AlSi10Mg alloy: process optimisation and mechanical properties development. *Mater. Des.* 65, 417–424.
- Rosenthal, I., Shneck, R., Stern, A., 2018. Heat treatment effect on the mechanical properties and fracture mechanism in AlSi10Mg fabricated by additive manufacturing selective laser melting process. *Mater. Sci. Eng., A* 729, 310–322.
- Rosenthal, I., Stern, A., Frage, N., 2017. Strain rate sensitivity and fracture mechanism of AlSi10Mg parts produced by Selective Laser Melting. *Mater. Sci. Eng., A* 682, 509–517.
- Rumelhart, D.E., Hinton, G.E., Williams, R.J., 1986. Learning representations by back-propagating errors. *Nature* 323, 533–536.
- Schmidhuber, J., 2015. Deep Learning in neural networks: an overview. *Neural Network* 61, 85–117.
- Schmidt, J., Marques, M.R.G., Botti, S., Marques, M.A.L., 2019. Recent advances and applications of machine learning in solid-state materials science. *npj Comput. Mater.* 5, 83.
- Takata, N., Kodaira, H., Suzuki, A., Kobashi, M., 2018. Size dependence of microstructure of AlSi10Mg alloy fabricated by selective laser melting. *Mater. Char.* 143, 18–26.
- Tancogne-Dejean, T., Roth, C.C., Woy, U., Mohr, D., 2016. Probabilistic fracture of Ti-6Al-4V made through additive layer manufacturing. *Int. J. Plast.* 78, 145–172.
- Tang, M., Pistorius, P.C., 2017. Anisotropic mechanical behavior of AlSi10Mg parts produced by selective laser melting. *JOM (J. Occup. Med.)* 69, 516–522.
- Thijss, L., Kempen, K., Kruth, J.P., Van Humbeeck, J., 2013. Fine-structured aluminium products with controllable texture by selective laser melting of pre-alloyed AlSi10Mg powder. *Acta Mater.* 61, 1809–1819.
- Wang, H., Dhiman, A., Ostergaard, H.E., Zhang, Y., Siegmund, T., Kružic, J.J., Tomar, V., 2019. Nanoindentation based properties of Inconel 718 at elevated temperatures: a comparison of conventional versus additively manufactured samples. *Int. J. Plast.* 120, 380–394.
- Wei, P., Wei, Z., Chen, Z., Du, J., He, Y., Li, J., Zhou, Y., 2017. The AlSi10Mg samples produced by selective laser melting: single track, densification, microstructure and mechanical behavior. *Appl. Surf. Sci.* 408, 38–50.
- Witzen, W.A., Polonsky, A.T., Pollock, T.M., Beyerlein, I.J., 2020. Three-dimensional maps of geometrically necessary dislocation densities in additively manufactured Ni-based superalloy IN718. *Int. J. Plast.*, 102709.

- Yan, S., Yang, H., Li, H., Yao, X., 2016. A unified model for coupling constitutive behavior and micro-defects evolution of aluminum alloys under high-strain-rate deformation. *Int. J. Plast.* 85, 203–229.
- Zaretsky, E., Stern, A., Frage, N., 2017. Dynamic response of AlSi10Mg alloy fabricated by selective laser melting. *Mater. Sci. Eng., A* 688, 364–370.
- Zhang, A., Mohr, D., 2020. Using neural networks to represent von Mises plasticity with isotropic hardening. *Int. J. Plast.*, 102732.
- Zhang, P., To, A.C., 2016. Transversely isotropic hyperelastic-viscoplastic model for glassy polymers with application to additive manufactured photopolymers. *Int. J. Plast.* 80, 56–74.
- Zhang, Y., Ling, C., 2018. A strategy to apply machine learning to small datasets in materials science. *npj Comput. Mater.* 4, 28–33.